VOL 101 No 3
September 2010

SAIEE Africa Research Journal

CBi electric
low voltage

Eskom

TUTORIAL PAPER

METAMATERIALS: CHARACTERISTICS, DESIGN AND MICROWAVE APPLICATIONS

Branka. Jokanović[*], Riana H Geschke[**], Theunis S Beukman[**] and Vojislav Milošević[*]

** Physics Institute, Belgrade, Serbia, E-mail: brankaj@ipb.ac.rs*

*** Department of Electrical and Electronic Engineering, Stellenbosch University, Stellenbosch, South Africa, E-mail: Riana@ieee.org*

Abstract: We present an overview of unique properties of metamaterials, especially negative index materials. These have allowed novel applications, concepts and devices to be developed in the past decade. A review of the progress made in this field is presented with a focus on microwave devices and applications in wireless communications. Since a metamaterial can be regarded as a continuous medium with effective dielectric permittivity and effective magnetic permeability, we present the procedure for the extraction of effective electromagnetic parameters for a guided wave structure with split-ring resonators. As examples, our own designs of bandpass and triple-band filters, which are constructed using metamaterial-inspired resonator elements, are presented and discussed.

Keywords: metamaterials, left-handed materials, negative-index of refraction materials, split-ring resonator

1. INTRODUCTION

Metamaterials are artificial, usually periodic structures which exhibit advantageous and unusual electromagnetic properties. According to [1], a metamaterial is defined as: "*an object that gains its electromagnetic material properties from its structure rather than inheriting them directly from the material it is composed of* ". The term metamaterial was also defined as "*macroscopic composites having a synthetic, three-dimensional, periodic cellular architecture designed to produce an optimized combination, not available in nature, of two or more responses to specific excitation* " [2,3].

The size of the unit cells of metamaterials is typically smaller than one tenth of the propagating signal wavelength. Due to the small size, it can be considered to form an effective medium with an effective dielectric permittivity and effective magnetic permeability which represents the bulk artificially constructed medium. By a proper design of constituent unit cells, the effective parameters of metamaterials can be made arbitrarily small or large, or negative.

Metamaterials are generally implemented in a periodic configuration although this is not a requirement. From a fabrication point of view it is easier to design and build by repeating a cell than by using different cells. Also, making metamaterials periodic allows one to use well-established theory of periodic structures, where a non-uniform structure would be much more difficult to analyze.

Possible properties of materials in the ε-μ domain are shown in Fig. 1. The first quadrant ($\varepsilon > 0$ and $\mu > 0$) of the ε-μ diagram in Fig. 1, represents right-handed materials (RHM), which support forward propagating waves.

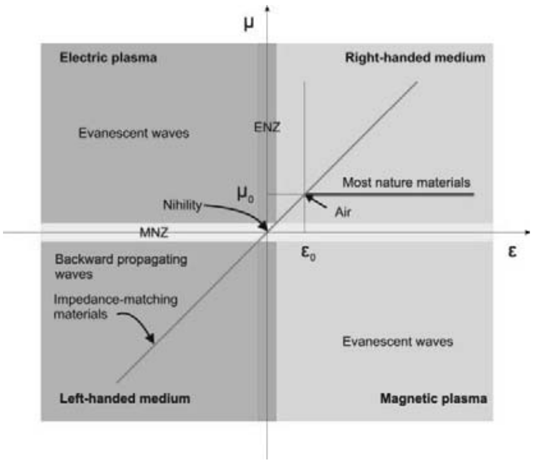

Figure 1. Possible properties of isotropic and lossless materials in the ε-μ domain. ENZ denotes an ε-near-zero material, while MNZ is a μ-near-zero material. Based on [2].

The blue line in Fig. 1 represents the materials found most commonly in nature with a permeability μ_0 and permittivity larger than ε_0. Although this is not always emphasized, even for a RHM the material properties typically vary with frequency. In this quadrant, the electric field **E**, the magnetic field **H**, and the wave vector **k** form a right-handed system, as described by Maxwell's equations.

The second quadrant ($\varepsilon < 0$ and $\mu > 0$) describes electric plasmas which support evanescent waves. The fourth quadrant ($\varepsilon > 0$ and $\mu < 0$) also supports evanescent waves. These are both single negative (SNG) quadrants, meaning that only one effective parameter is negative.

The third quadrant (ε < 0 and μ < 0 or double negative (DNG)) contains the left-handed materials, which were proposed in 1967 [4]. In LHM, the electric field **E**, the magnetic field **H**, and the wave vector **k** form a left-handed system and these support "backward" propagating waves. The term backward refers to the opposite sign of group and phase velocity. The index of refraction $n = \sqrt{\varepsilon_r \mu_r}$ is negative.

Nature favours conventional RHM (quadrant 1) which can exist at any frequency, and to lesser extent single negative (SNG) materials (quadrants 2 and 4), available only in restricted frequency bands. Yet the laws of physics do not prohibit the existence of LH materials. This provides the third quadrant of the ε-μ diagram in Fig. 1. In order to satisfied the generalized entropy conditions, LH materials need to be frequency dispersive, i.e. their propagation constant β has to be a nonlinear function of frequency.

Most of the initial interest in the metamaterial field was directed at investigating materials in the third quadrant. Although metamaterials were first known as left-handed materials (LHMs) or negative index materials (NIMs), the metamaterial concepts includes much more than the LHM which occur in the third quadrant. Disadvantages are that devices based on LHM are usually narrow band and display high losses.

Not all work in the metamaterial field is concentrated on LHM or DNG materials. For example, the point $\mu = -\mu_0$ and $\varepsilon = -\varepsilon_0$ represents anti-air in the LHM region, which will produce a perfect lens; the point μ = 0 and ε = 0, the zero refractive index point or nihility, which finds application in the design of highly directive antennas and also multiband antennas [5]; the line μ = ε in both RHM and LHM regions represents impedance matching materials, which have perfect impedance matching with air, resulting in no reflections. Also, the vicinity of μ = 0 is called as μ-near-zero (MNZ) material, and the vicinity of ε = 0 is a ε-near-zero (ENZ) material [2]. Both these have special applications such as supercoupling, squeezing energy and field confinement in narrow channels [6], [7]. Various applications were demonstrated for small antennas using electrically small dipoles with SNG or DNG shells to improve the antenna efficiency [5].

The development of metamaterials started with a Russian scientist, Veselago [4], who speculated about the theory of LHM and the possible properties in his paper titled "*The electrodynamics of substances with simultaneously negative values of* ε *and* μ". The paper was first published in Russian in 1967 and a year later in English.

Figure 2. The array of split-ring resonators plus wire assemblies used for the experiment. Adopted from [11].

The next milestone was the introduction by Pendry of a thin wire structure as a negative-ε medium by decreasing plasma frequency into microwave range [8] and a negative-μ split-ring resonator structure [9] operating in microwave range. Smith et al [10,11] then combined the thin wire structure with split-ring resonators to demonstrate experimentally that a LH structure can be implemented in the microwave frequency range. This is shown in Fig. 2. The split-resonant type metamaterial elements are discussed in section 3.1.

Eleftheriades [12], Caloz and Itoh [13], and Oliner [14] did similar work around the same time and introduced non-resonant, low-loss and broad-bandwidth, transmission line (TL) metamaterials. Their approach is discussed in more detail in section 3.2.

Smith et al [15] introduced the gradient refraction index medium to continuously bend electromagnetic waves, which is different from metamaterials where the elements are all identical (e.g. Fig. 2). In the gradient material the properties vary with position, to obtain a refractive index that also varies with position. Pendry proposed an optical transformation in 2006 which find application in invisibility cloaks to control the propagation of electromagnetic waves [16].

Twelve books and one new journal on metamaterials have been published since 2003:

- S. Zouhdi, A. Sihvola and M. Arsalane, *Advances in Electromagnetics on Complex Media and Metamaterials,* Springer 2003.
- S. Tretyakov, *Analytical Modelling in Applied Electromagnetics*, Artech House, 2003.
- G. V. Eleftheriades and K. G. Balmain, *Negative-Refraction Metamaterials: Fundamental Principles and Applications,* Wiley-IEEE Press, 2005.
- C. Caloz and T. Itoh, *Electromagnetic Metamaterials: Transmission Line Theory and Microwave Applications*, Wiley-IEEE Press, 2006.
- N. Engheta and R. W. Ziokowski, *Metamaterials: Physics and Engineering Explorations*, Wiley-IEEE Press, 2006.
- Sir J. B. Pendry, *Fundamentals and Applications of Negative Refraction in Metamaterials*, Princeton University Press, 2007.
- R. Marques, F. Martin and M. Sorolla, *Metamaterials with Negative Parameters*, Wiley, 2007.

- C. M. Krowne and Y. Zhang, *Physics of Negative Refraction and Negative Index Materials, Optical and Electronic Aspects and Diversified Approaches*, Springer, 2007.
- S. A. Ramakrishna and T. Grzegorczyk, *Physics and Applications of Negative Refractive Index Materials*, SPIE and CRC Press, 2009.
- B. A. Munk, *Metamaterials: Critique and Alternatives*, Wiley, 2009.
- T. J. Cui, D. R. Smith, R. Liu, *Metamaterials Theory, Design and Applications,* Springer 2010.
- W. Cai, V. Shalaev, *Optical Metamaterials, Fundamentals and Applications*, Springer, 2010.
- A new Elsevier journal titled "Metamaterials" [17] was founded in 2007.

2. GENERAL PROPERTIES

Several physical phenomena are reversed in LH media and at the intersection between LH and RH media. This is due to the opposite sign of phase and group velocities. These are the Doppler effect, Vavilov-Čerenkov radiation, Snell's law, Goos-Hänchen effect, lensing effect (convex lenses produce diverging rays, which is opposite to RH lenses), and sub-wavelength focusing of an image by a flat slab. Some of these effects are illustrated in Fig. 3.

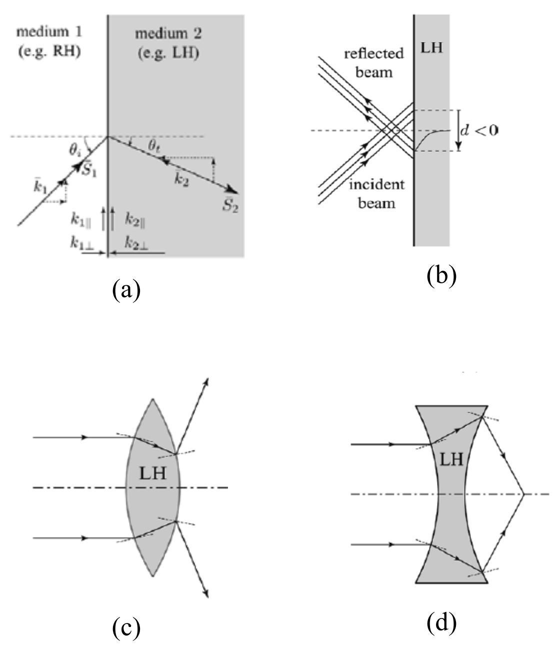

Figure 3. Reversed phenomena in LH metamaterials: (a) Snell's law, (b) Goos-Hänchen effect, (c) concave LH lens diverges, (d) convex LH lens converges. Adopted from [18].

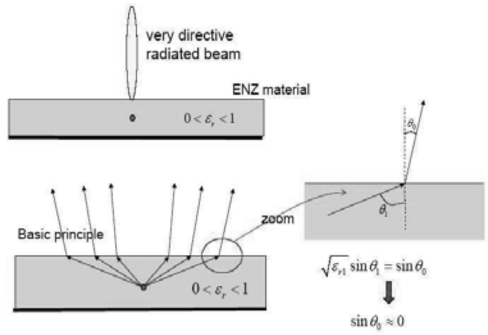

Figure 4. Application of an epsilon near-zero (ENZ) metamaterials in design of a small antenna with high directivity.

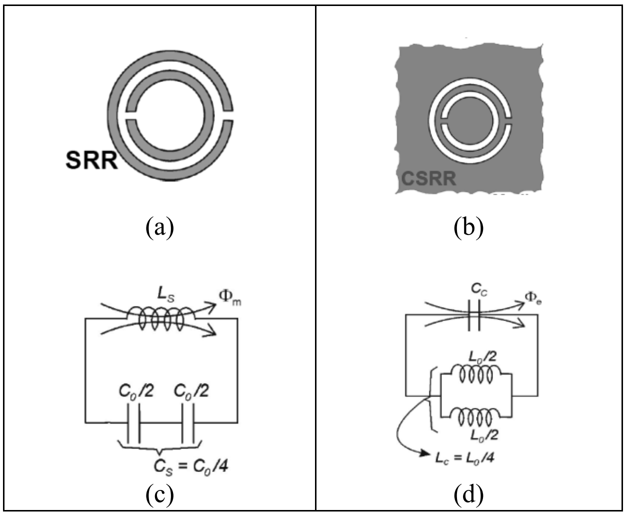

Figure 5. Split-ring resonator (SRR) (μ < 0) and complementary split-ring resonator (CSRR) (ε < 0) and equivalent circuits. Adopted from [40].

Besides LH materials, metamaterials with a permittivity very close to zero (ENZ) can find very useful applications in design of small antennas with a very high directivity, as shown in Fig. 4. To achieve high directivity a classical antenna design requires an electrically large antenna, but if the antenna source is placed in ENZ MMs, all radiation can be focused in the direction which is almost normal to the interference between
air and the ENZ MM, since index of refraction of ENZ media is close to zero. It follows from Snell's law that in Fig. 4, $\theta_0 \approx 0$:

$$n_1 \sin\theta_1 = n_0 \sin\theta_0 \quad (1)$$

3. MICROWAVE APPLICATIONS

Applications of LH metamaterials (MMs) in microwaves are numerous and opened the door to new strategies in design of microwave devices, also referred to as dispersion engineering, which considers and controls the phase response of devices.

There are two main approaches in design of microwave circuits using metamaterials: the *resonant approach* which uses thin wires, split-ring resonators (SRRs) and complementary split-ring resonators (CSRRs) [19], [20] and the *transmission line approach* [21] based on dual transmission line theory. The first one leads to lossy and narrow-band circuits, while the second, non-resonant approach, provides design tools for broad bandwidth devices with low loss.

3.1 Resonant Approach

Split-ring resonators exhibit extreme values of magnetic permeability in the vicinity of quasi-static resonant frequency, when they are excited by means of an axial magnetic field. They behave as an LC resonant tank as it is shown in Fig. 5(a). Although having a narrow frequency range with negative permeability, SRR based configurations attracts a lot of attention. In microstrip technology, SRRs can only be etched in the upper substrate side, next to the microstrip line. Array of SRRs exhibits filtering properties, and when properly polarized, can reject signal propagation.

The complementary split-ring resonator (CSRR) is the dual of the SRR, by the Babinet principle. The CSRR has metallization removed from the ground plane to form the inverse shape to that of the SRR. CSRRs are normally placed adjacent or directly underneath microstrip lines. Interesting filter applications have been demonstrated using CSRRs [20,22]. Periodic gaps in the microstrip line, together with the CSRR, produce a LH response in a narrow frequency band.

Other small elements useful for miniaturization have also been proposed, for example the broadside coupled split-ring resonator (BC SRR) [23], the spiral resonator (SR), [24,25], multiple CSRRs [26] and square Sirpinski fractal CSRRs [27].

Fig. 6 shows a LH microstrip line loaded with CSRRs which provide a negative permittivity, while capacitive gaps in microstrip line give a negative permeability. This line acts as a passband filter since both ε and μ are both negative in the passband.

3.2 Transmission Line (TL) Approach

Transmission line theory has always been a useful tool for analysis and design of microwave circuits. The homogeneous models of pure RH and LH lossless transmission lines are shown in Fig. 7 (a).

It can be seen that the LH TL introduced in Fig. 7(a) on the right, is the dual of the RH TL, i.e. the RH TL is a low pass filter, while the LH TL is a high pass filter. The average unit cell size is represented by Δz and can be much smaller than λ_g, at should be at least less than $\lambda_g/4$. In reality, a pure LH TL cannot exist due to the inevitable RH parasitic series inductance and parasitic capacitance. Therefore, a Composite right and left-handed CRLH TL in Fig. 6 (b) (RH parasitic contribution is denoted in red) is the most general representation of the structure with LH attributes in some frequency bands.

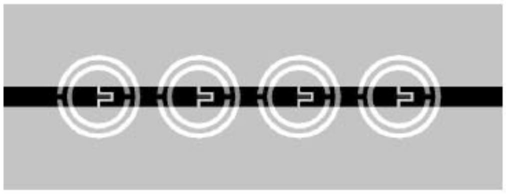

Figure 6. Microstrip line (black) with CSRRs etched in ground plane (gray). Capacitive gaps have been etched on the strip to obtain a left-handed passband. Adopted from [20].

Therefore, a Composite right and left-handed CRLH TL in Fig. 7(b) (RH parasitic contribution is denoted in red) is the most general representation of the structure with LH attributes in some frequency bands.

The CRLH TL exhibits a stop band in the β-diagram between $\omega_{\Gamma 1}$ and $\omega_{\Gamma 2}$ (Fig. 7(b)), which do not exist in pure RH and LH TLs. In the case where shunt and series resonances are equal:

$$L_R^{'} C_L^{'} = L_L^{'} C_R^{'} \qquad (2)$$

The RH and LH contributions exactly balance each other at the given frequency ω_0 and the stop band is removed. This condition is referred to as the *balanced case*.

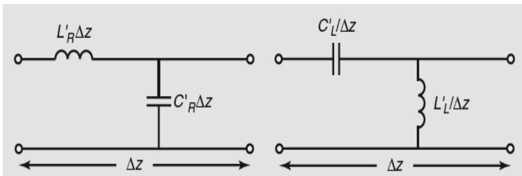

(a)

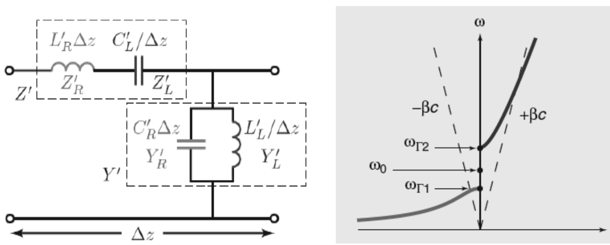

(b)

Figure 7. Equivalent circuit models of: (a) homogeneous RH and LH transmission line, (b) Composite right/left handed (CRLH) TL with β-diagram. The LH band is red and the RH band is blue. Adopted from [21]

The phase constant splits distinctly into two parts β_L and β_R at the frequency ω_0. At that frequency β becomes equal to zero, which means that guided wavelength becomes infinite

$$\lambda_g = \frac{2\pi}{|\beta|} \qquad (3)$$

An example of composite right/left handed microstrip line, which is loaded with non-resonant elements like interdigital capacitors and shunt inductors connected to ground is shown in Fig. 8.

Although, at first glance, the resonant and transmission line approaches look very different, they belong to the same *generalized transmission line theory of metamaterials* [28]. To obtain a desired phase response, transmission line can be loaded either with lumped inductance and capacitance (TL approach), or with SRRs and CSRRs which behave as a quasi-lumped elements (resonant approach). It was shown that balanced case and broadband behaviour is not unique characteristics of metamaterials designed by TL approach. They are also realizable with resonant type unit cells as CSRRs, which are coupled to a host transmission line [29].

3.3 Basic advantages of MMs

The main relevant aspect of MMs is the possibility of implementing miniaturized components due to the small electrical size of its constitutive elements, together with improved performance related to its unique and controllable dispersion characteristics. This offers new challenges for the design of inexpensive 1-D and 2-D beam-scanning antennas without phase-shifters and small multi-band antennas with superior performance and low cost, that is not easy achievable through established approaches.

The essential advantages of the MM-based technology are the following:

- Extremely small unit cells resulting in super-compact resonators,
- Zeroth-order resonance existing in LH metamaterials, resulting in small antennas whose resonance is independent of the physical length,
- Zero phase-shift on any length of LH transmission line, when operated at the transition frequency between RH and LH region, resulting in less complex antenna feeding networks,
- Multi-band concept of CRLH TL, resulting in arbitrary (non-harmonic related) choice of operating frequencies of multi-band devices,
- Electrical controllability of unit cells resulting in reconfigurable microwave devices,
- Fabrication using conventional technologies and low cost materials resulting in cost effective microwave devices and antennas.

Multiband operation at arbitrary, nonharmonic related frequencies becomes possible due to nonlinear phase characteristics of a CRLH TL [30], as illustrated in Fig. 9. It can be seen that the dual-band filter has first and second passbands located at the frequencies f_0 and $3f_0$ for the conventional right-handed (RH) line consisting of quarter-wavelength resonators. If we replace the RH line with the CRLH TL, the amplitude response of the filter (Fig. 9(a)) can be mapped to the amplitude response shown in Fig. 9(c) via nonlinear phase response of CRLH TL (Fig. 9(b)). The corresponding position of the centres of passbands f_1 and f_2 can be arbitrarily spaced depending only on the engineered phase response.

Some applications of MMs include dual-band and enhanced-bandwidth microwave devices such as couplers, phase shifters, power dividers [31], mixers, super-compact (i.e. super slow-wave) structures, zeroth-order resonators with constant field distribution [32], tightly coupled-line phase/impedance couplers [33], and series-fed linear array with reduced beam squint [33], which increases scanning range from 2.67 GHz for conventional delay line to 10.44 GHz for metamaterial line, giving an improvement of 290%.

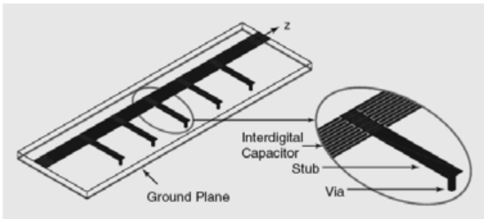

Figure 8. Microstrip composite right/left handed line consisting of interdigital capacitors and shorted stub inductors. Adopted from [21].

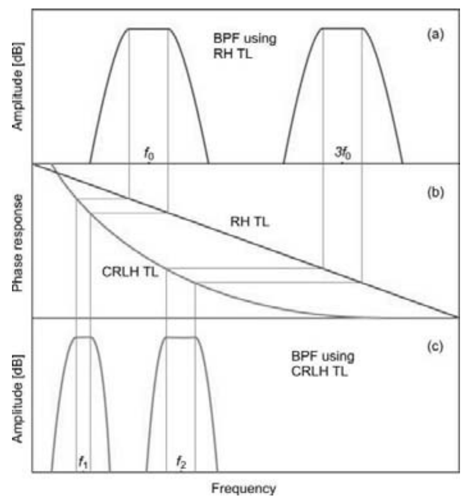

Figure 9. (a) The amplitude response of the conventional bandpass filter, (b) The phase response of RH transmission line and composite right-left handed line, (c) The amplitude characteristic of dual-band filter with nonharmonic related band spacing. Adopted from [30].

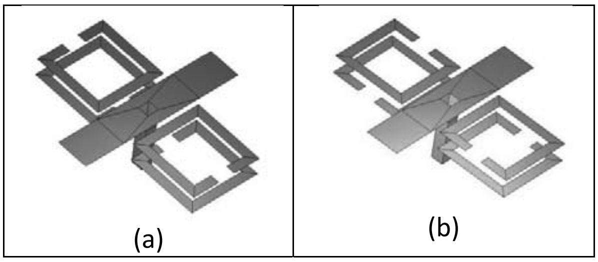

Figure 10. (a) Basic configuration of metamaterial's unit cell, (b) SRRs are rotated by 90 degrees.

4. EXTRACTION OF EFFECTIVE PARAMETERS

To characterize metamaterials, the effective medium theory is used since the wavelength of excitation is much longer than the dimensions of the constituent elements. Here we present the effective parameter extraction for a 1-D LH microstrip line consisting of the periodically loaded thin wires and split-ring resonators (SRRs) along the two-layer microstrip line [35].

The electromagnetic parameter extraction is based on the idea of replacing the unit cells of a metaline by an equivalent microstrip line with homogeneously filled effective permittivity ε_{eff} and permeability μ_{eff}. The fields in the equivalent structure should be equal to the mean fields in the original structure. The equivalent microstrip line has the same line width as an original one and also the same substrate thickness. Effective parameters can be extracted from either simulated or measured scattering parameters. This method is applicable to the unit cells which are symmetrical in respect to the inputs, i.e. only if s_{11} is equal to s_{22} [36].

The propagation constant γ can be determined by a Bloch wave analysis:

$$\gamma = \pm\frac{1}{L}\cosh^{-1}\frac{1-s_{11}^2+s_{21}^2}{2s_{21}} = \pm\frac{\omega}{c}\sqrt{\mu_{efff}\,\varepsilon_{eff}} \qquad (4)$$

To determine ε_{eff} and μ_{eff} another equation for z_{eff} is used:

$$z_{eff} = \sqrt{\frac{\mu_{eff}}{\varepsilon_{eff}}} = \left(\frac{1+\Gamma}{1-\Gamma}\right)\frac{Z^{TL}}{Z_a^{TL}} \qquad (5)$$

where Γ is obtained by Nicholson-Ross-Weir approach [37]:

$$\Gamma = k \pm \sqrt{k^2-1} \qquad (6)$$

$$k = \frac{s_{11}^2 - s_{21}^2 + 1}{2(s_{21})} \qquad (7)$$

Parameter extraction is applied to the unit cells consisting of two pairs of identical split-ring resonators (SRRs) realized on two-layer substrate (h_1=0.635 mm, h_2=1.575 mm, ε_{r1}=10.2, ε_{r2}=2.2) and coupled to microstrip line. The vertical via is placed in the middle between top SRRs and bounded to the microstrip conductor and ground plane. The basic configuration (Fig.10(a)) consists of two

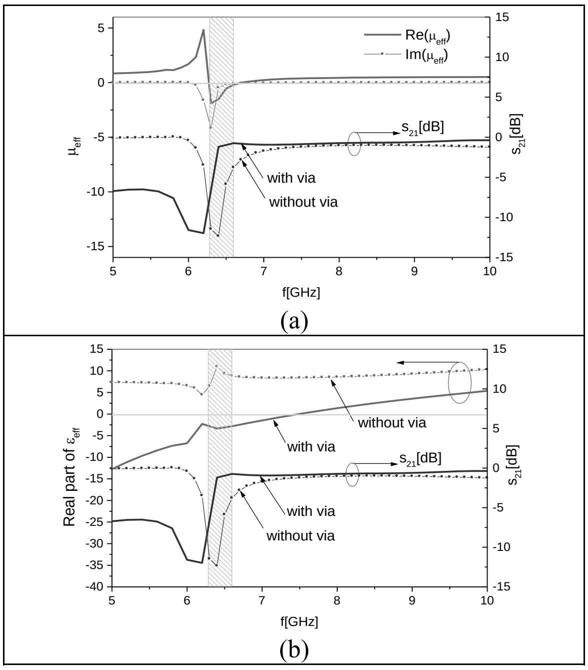

Figure 11. Influence of via for the configuration shown in Fig. 8 (a): (a) the effective μ is unaffected by via, (b) the effective ε becomes positive without via. Region with negative effective μ is denoted by patterned rectangular bar.

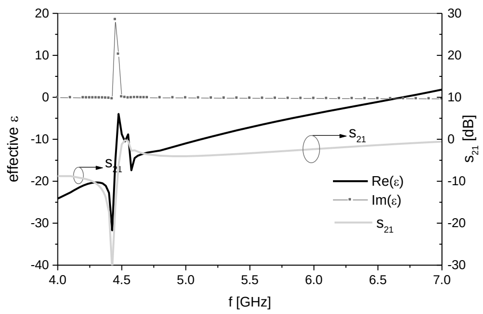

Figure 12. Effective permittivity for the unit cell in Fig. 8 (b).

identical square SRRs on the top of substrate 1 which are coupled with two bottom SRRs on the top of substrate 2. The bottom SRRs have the splits oriented opposite to the above ones. The second unit cell is shown in Fig. 10(b) and consists of SRRs twisted by 90 degrees with respect to basic unit cell. The structure is analyzed using 3D electromagnetic solver Wipl-D Pro v7.1, based on a method of moments (MoM) [38].

The parameter extraction procedure is used to investigate the influence of via for the configuration in Fig. 10(a). The results for a unit cell with and without via are shown in Fig. 11. It was shown that the via did not have any effect on extracted effective permeability, but due to the absence of a via, the real part of the effective permittivity becomes positive. Also, it is shown that the structure has a passband only in the region where both effective parameters (their real parts) are negative, i.e. in frequency range 4.4-4.68 GHz.

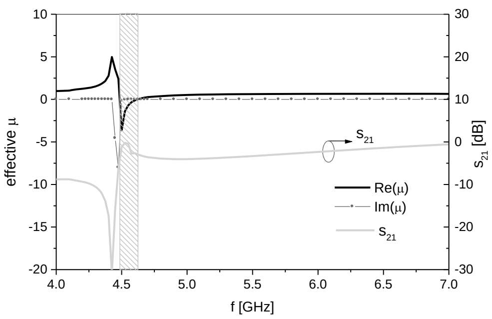

Figure 13. Effective permeability for the unit cell shown in Fig. 8 (b). The rectangular bar denotes frequency range where effective μ is negative.

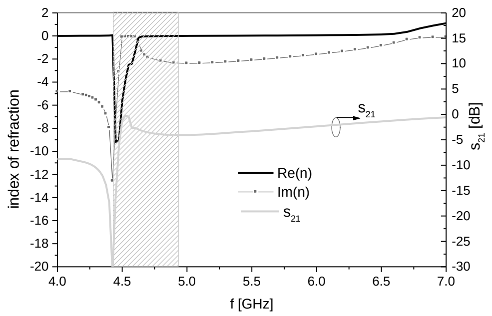

Figure 14. Extracted index of refraction. The rectangular bar denotes the frequency range with negative real part of the refractive index.

The index of refraction is negative in a wider range, for frequencies between 4.33-4.87 GHz, which indicates the existence of region with single negative refractive index.

Veselago showed in his paper [5] that a material with simultaneously negative permeability and permittivity has a negative refractive index. However, this is actually a strong (sufficient) condition. The necessary condition is given by [39]:

$$\varepsilon'|\mu| + \mu'|\varepsilon| < 0 \tag{8}$$

This leads to negative real part of the refractive index. Following from the previous discussion, two types of NIMs can be introduced. Double NIM (DN-NIM) has both ε' < 0 and μ' < 0. A single NIM (SN-NIM) has a negative refractive index with either $\mu' < 0$ or $\varepsilon' < 0$ (but not both). The ratio $|n'|/n''$ is a figure of merit (FOM) and it is always higher for DN-NIMs.

Figs. 12-14 show the extracted effective parameters for the unit cell in Fig. 10(b). The structure exhibits a negative real part of refractive index in the frequency range 4.4-4.9 GHz. The imaginary part of the refractive index is equal to zero in the range 4.5-4.6 GHz which coincides with the range of negative effective permeability. This determines the range of DN-NIM. The index of refraction is positive, but very low (about 0.2) up to 6.7 GHz, at the frequency where the effective permittivity becomes positive (Fig. 14).
Even though the unit cells from Fig. 10 are mutually different, due to SRRs twisted by 90 degrees, the extracted parameters are very similar, even the range where effective permeability is positive and the refractive index is negative.

When split ring resonators are coupled with a microstrip line it is usually done with the configuration from Fig. 10(a), but our simulations and parameter extraction show that both configurations from Fig. 10 exhibit about the same characteristics. The only difference observed is a somewhat increased range of negative permittivity up to 7.28 GHz for the basic configuration. Below this frequency, the refractive index is positive, but very small (about 0.24).

5. COMPACT METAMATERIAL-INSPIRED DEVICES

Split-ring resonators (as described in Section III) originate from [9] and was used in [10,11] with arrays of wires to obtain and demonstrate a negative index of refraction. Split-ring resonators (SRR) and spiral elements are also used as resonator elements in filters, power dividers and couplers [40]-[44]. The SRR consists of two concentric rings with splits on opposite ends. This is a configuration that provides relatively high coupling between the two rings. A simple equivalent circuit is also shown in Fig. 5. These structures provide very efficient ways to obtain miniaturization. Variations on the basic geometry can provide even better miniaturization in for example filters [46] and couplers [44].

5.1 Couplers with Metamaterial Elements

The hybrid coupler of Fig. 15 demonstrates the use of LH and RH unit cells to construct artificial lines with specified phase shifts. The 270° degree line length required in the coupler is replaced by a LH line with phase shift of -90°, which is much shorter. The device is about 3 three times smaller than a conventional design.

Another example is found in [45] using a multilayer low temperature co-fired ceramic (LTCC) technology. Here artificial lines are employed, constructed using quasi-lumped elements. Also in this work [45], a dual-band directional coupler is demonstrated. These devices are about 4 times smaller than conventional design, with good performance.

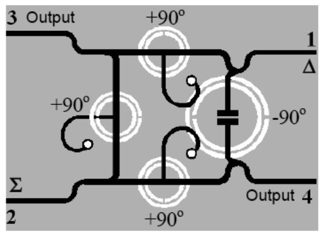

Figure 15: The layout for the hybrid coupler using left-handed (LH) and right-handed (RH) unit cells, adopted from [44].The white rings are on the bottom layer and indicate removed copper.

5.2 Cross-coupled Spiral Resonator (SR) Filter

The filter design (Fig. 16) places zeros in the transmission coefficient at finite frequencies. This is achieved by introducing cross-coupling between the input and output SRs of the filter. The simulated and measured responses are given in Fig. 17. The filter is designed to operate at 2.4 GHz (measured 2.32 GHz) with a Chebyshev response with a fractional bandwidth of 10% (measured 11%). A Taconic substrate with a relative permittivity of 2.2 is used. We found a frequency shift from the predicted response due to tolerances in the manufacturing process. In all filters with such small spacing dimensions between rings (between 100 and 200 microns), a very high precision manufacturing process is required.

It is customary to compare filter dimensions (without feed) as the size in guide wavelengths λ_g. Conventional microstrip filters such as the combline has typical dimensions of $\lambda_g/4 \times \lambda_g/4$ for a fourth order filter.

The dimensions of the cross-coupled fourth order SR filter is $\lambda_g/6.5 \times \lambda_g/6.5$ or 1.6 times smaller than a conventional filter and the introduced transmission zeros in the response result in steeper attenuation slopes than the standard Chebyshev response.

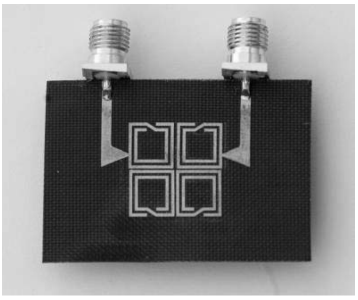

Figure 16: The fourth order cross-coupled SR filter.

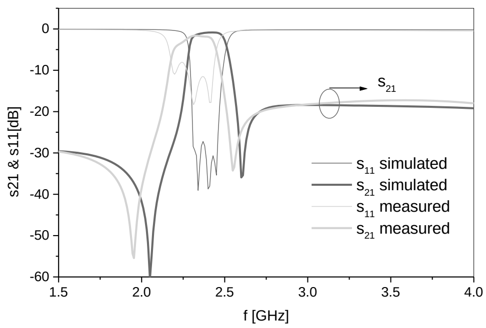

Figure 17: The S-parameters of the simulated and measured filters. The shift in frequency is due the manufacturing process. This filter has very small gaps between rings and requires high-manufacturing precision.

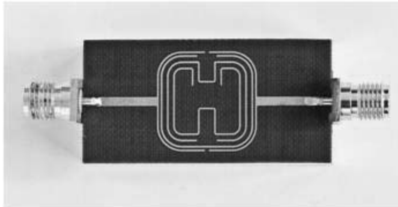

Figure 18: Triple-band SRR resonator with three nested split-ring resonators. Dimensions are w_1=0.6mm, w_2=0.4, w_3=0.4 and g=0.4mm, substrate relative permittivity of 2.2 and substrate thickness 0.76mm.

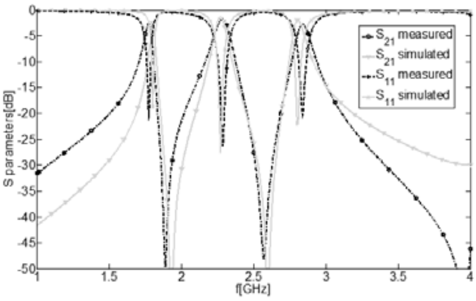

Figure 19: The S-parameters of the simulated (solid lines) and measured (dotted lines) filter. Three passbands with equal spacing are seen. The transmission response demonstrates zeros between passbands.

5.3 Multiband Split-ring Resonators for Filters

Most split-ring resonators have two nested rings (Fig. 5) where the second ring is used to couple strongly to the first and lower the fundamental resonant frequency, thereby providing the miniaturization effect. This produces a spurious pass-band quite close to the main one, and is a liability in some cases.

However, for a dual band or triple-band response, nested resonators are very suitable. Each ring provides an alternative propagation path between the input and output port and can be used to position transmission zeros, thereby constructing separate pass-bands. The possibility to add more rings is limited by the space required to nest the rings. In Fig. 18 we show our composite resonator with three nested split-ring resonators to obtain a triple-band response [46]. For equal mode spacing, the three resonators must have identical resonant frequencies and identical coupling. To fit the inner rings, length corrections are inserted to adjust the resonances. More detail on this type of resonator and design is given in [46].

The simulated and measured response for the filter of Fig. 18 is shown in Fig. 19. The three measured pass-bands are found at 1.775 GHz, 2.283 GHz and 2.873 GHz with insertion losses of 2.6 dB, 1.77 dB and 2.72 dB. The measured unloaded resonator Q-factors are 138, 121 and 114, which are typical for this type of microstrip openring resonators. The composite resonator, which is a third order filter with three passbands, has dimensions $\lambda_g/6.5 \times \lambda_g/6.5$.

CONCLUSION

Metamaterials present a new paradigm in electromagnetics and have attracted great interest in the past ten years. Among metamaterials, negative refractive index materials or left-handed materials have drawn special attention in microwaves. Both resonant and non-resonant types of metamaterials found applications and opened new design strategies in miniaturization, multiband operation, and reconfigurability of microwave devices and antennas. Some new phenomena like zeroth-order resonance, zero phase-shift on arbitrary lengths of LH transmission lines at the transition frequency between RH and LH regions were discovered. From the progress and interest in this field it is clear that the future of metamaterials lies in the field of optics. This is closely linked to advancements in nanotechnology.

ACKNOWLEDGMENT

This work is partly supported by Serbian Ministry of Science and Technological Development through project TR-1009, “Dual-Band and Triple-Band Metamaterial-Based Microwave Devices and Antennas for Modern Communication Systems”.

The authors would like to thank WIPL-D Software for the license and support in advanced modelling of unit cells in section III, and also FEKO for the license and support for the design of the two filters in section IV.

REFERENCES

[1] A. Sihvola, “Metamaterials in electromagnetics”, Metamaterials, vol. 2, 2007.

[2] T. J. Cui, D. R. Smith, R. Liu, *Metamaterials: Theory, Design and Applications*, Springer, 2009.

[3] W. S. Weiglhofer, A. Lakhtakia, “Introduction to complex mediums for optics and electromagnetics”, SPIE Press, Bellingham, WA, USA, 2003.

[4] V. Veselago: “The electrodynamics of substances with simultaneously negative values of μ and ε”, *Soviet Physics Uspekhi*, vol. 92, no. 3, pp. 517-526, 1967.

[5] R. W. Ziolkowski, “Metamaterial-based antennas: research and developments”, *IEICE Trans. Eectron.*, vol. E890C, no. 9, Sept. 2006.

[6] B. Edvards, A. Alu, M. E. Young, M. G. Silveirinha and N. Engheta, “Experimental verification of epsilon-near-zero metamaterial coupling and energy squeezing using a microwave waveguide”, *Physical Review Letters* 100, 033903 (2008).

[7] A. Alu and N. Engheta, “Dielectric sensing in ε-near-zero narrow waveguide channels”, *Physical Review B* 78, 045102 (2008).

[8] J. B. Pendry, A. J. Hoden, W. J. Stewart and I. Youngs, “Extremly low frequency plasmons in metallic mesostructures”, *Physical Review Letters*, vol. 76, num. 25, pp. 4773-4776, 17 June 1996.

[9] J. B. Pendry, A. J. Holden, D. J. Robbins and W. J. Stewart “Magnetism from conductors and enchanced nonlinear phenomena”, *IEEE Trans. Microwave Theory Tech.*, vol. 47, no. 11, pp. 2075-2084, November 1999.

[10] R. A. Shelby, D. R. Smith, S. Schultz: “Experimental verification of a negative index of refraction”, *Science*, vol. 292, pp. 77-79, 2001.

[11] D .R. Smith, W. J. Padilla, D. C. Vier, S. C. Nemat-Nasser and S. Schultz, “Composite medim with simultaneously negative permeability and permittivity”, *Phys. Rev. Lett.* vol. 84, no. 18, pp. 4184-4187, May 2000.

[12] A. K. Iyer and G. V. Eleftheriades, “Negative refractive index metamaterials supporting 2-D waves”, in Proc. *IEEE MTT Int. Symp.* 2002, vol. 2, pp. 412-415.

[13] C. Caloz and T. Itoh, “Application of the transmission line theory of left-handed (LH) materials to the realization of a microstrip LH transmission line”, in Proc. IEEE-AP-S USNC/URSI *National Radio Science Meeting* 2002, vol. 2, pp. 412-415.

[14] A. A. Oliner, “A periodic-structure negative-refractive-index medium without resonant elements”, in URSI Dig., IEEE-AP-S USNC/URSI *National Radio Science Meeting* 2002, vol. 2, pp.41.

[15] D. R. Smith, J. J. Mock, A. F. Starr, D. Schuring, “Gradient index metamaterials”, *Phys. Rev. E*, 71, 036609 (2005).

[16] J. B. Pendry, D. Schuring, D. R. Smith, “Controlling electromagnetic fields”, *Science*, 312, 1780 (2006).

[17] M. Lapine, “Editorial: the age of metamaterials”, *Metamaterials*, vol 1, 2007.

[18] C. Caloz and T. Itoh, “Metamaterials for High-Frequency Electronics”, Proceedings of the IEEE, vol. 93, no. 10, October 2005, pp. 1744-1752.

[19] F. Martín, F. Falcone, J. Bonache, R. Marqués and M. Sorolla, “Miniaturized coplanar waveguide stop band filters based on multiple tuned split ring resonators”, *IEEE Microwave Wireless Comp. Lett.*, vol. 13, pp. 511-513, December 2003.

[20] F. Falcone, T. Lopetegi, M.A.G. Laso, J.D. Baena, J. Bonache, R. Marqués, F. Martín, M. Sorolla, “Babinet principle applied to the design of metasurfaces and metamaterials”, *Phys. Rev. Lett.*, vol. 93, p 197401, November 2004.

[21] A. Lai, C. Caloz and T. Itoh, “Composite Right/Left Handed Transmission Line Metamaterials”, *IEEE Microwave Magazine*, Sept. 2004, pp. 34-50.

[22] R. Marques, J. D. Baena1, M. Beruete, F. Falcone, T. Lopetegi, M. Sorolla, F. Martın and J. Garcia, “*Ab initio* analysis of frequency selective surfaces

based on conventional and complementary split ring resonators", *J. Opt. A: Pure Appl. Opt.* 7 (2005) S38–S43 Januray 2005.

[23] R. Marqués, F. Medina, and R. R.-E. Idrissi, "Role of bianisotropy in negative permeability and left handed metamaterials", Phys. Rev. B, Condens. Matter, vol. 65, pp. 144 441–144 446, Apr. 2002.

[24] J. Baena, R. Marqués, F. Medina, and J. Martel, "Artificial magnetic metamaterial design by using spiral resonators", *Phys. Rev. B*, Condens. Matter, vol. 69, pp. 14 402–14 402, Jan. 2004.

[25] F. Falcone, F. Martín, J. Bonache, M. A. G. Laso, J. García-García, J. D. Baena, R. Marqués, and M. Sorolla, "Stopband and band pass characteristics in coplanar waveguides coupled to spiral resonators", *Microwave Opt. Technol. Lett.*, vol. 42, pp. 386–388, Sep. 2004.

[26] V. Crnojevic-Bengin, V. Radonic and B. Jokanovic, "Left-handed microstrip lines with multiple complementary split-ring and spiral resonators", *Microwave and Optical Tech. Letters*, vol. 49, no.6, pp.1391-1395, June 2007.

[27] V. Crnojevic-Bengin, V. Radonic and B. Jokanovic, "Fractal Geometries of Complementary Split-Ring-Resonators", *IEEE MTT Trans.* vol. 56, no. 10, October 2008, pp. 2312-2321.

[28] G.V. Eleftheriades, "A Generalized Negative-Refractive Index Transmission-Line (NRI-TL) Metamaterial for Dual-Band and Quad-Band Applications", IEEE Microwave Wireless Compon. Lett., Vol. 17, No. 6, pp. 415-417, June 2003.

[29] M. Gil, J. Bonache, J. Selga, J. Garcia-Garcia, F. Martin, "Broadband Resonant-Type Metamaterial Transmission Lines", IEEE Wireless Comp. Letters, Vol. 17, No.2, pp. 97-99, February 2007.

[30] C. H. Tseng and T. Itoh, "Dual-Band Bandpass and Bandstop Filters Using Composite Right/Left-Handed Metamaterial Transmission Lines," *International Microwave Symposium*, San Francisco, IMS 2006, pp. 931-934.

[31] M. Antoniades and G. V. Eleftheriades, "A Broadband Series Power Divider Using Zero-Degree Metamaterial Phase-Shifting Lines", *IEEE MWCL*, Nov. 2005.

[32] A. Sanada, C. Caloz and T. Itoh, "Zeroth order resonance in composite right/left handed transmission line resonators", *Pacific Microwave Conference*, Seoul, Korea, 2003, vol. 3, pp. 1588-1592.

[33] C. Caloz, A. Sanada and T. Itoh, "A novel composite rght/left handed coupled-line directional coupler with arbitrary coupling level and broad bandwidth", *IEEE Trans. Microwave Theory and Tech.*, vol. 52, pp. 980-992, Mar. 2004.

[34] G. V. Eleftheriades and M. Antoniades, "Antenna applications of negative-refractive-index transmission-line (NRI-TL) structures", *IET Microwaves, Antennas and Propagations*, Special Issue on Metamaterials, pp. 12-22, Feb. 2007.

[35] Shau-Gang Mao, Shiou-Li Chen, Chen-Wei Huang, "Effective Electromagnetic Parameters of Novel Distributed Left-Handed Microstrip Lines", *IEEE Trans. Microwave Theory Tech.*, vol. 53, no. 4, pp. 1515-1521, Apr. 2005.

[36] S. Ponjavic, B. Jokanovic, R. Geschke, "Extraction of Effective Electromagnetic Parameters of Microstrip Complementary Split-Ring Resonators, 3rd *International Congress on Advanced Electromagnetic Materials in Microwaves and Optics, Metamaterials 2009*, 30th August – 4th September, London.

[37] William B. Weir, "Automatic Measurement of Complex Dielectric Constant and Permeability at Microwave Frequencies", *Proceedings of the IEEE*, vol. 62, no. 1, Jan. 1974.

[38] http://www.wipl-d.com.

[39] R. A. Depine and A. Lakhtakia, "A new condition to indentify isotropic dielectric-magnetic materials displaying negative phase velocity", *Microwave and Optical Technology Letters*, vol. 41, no. 4, May 2004, pp. 315-316.

[40] J.D. Baena et al, "Equivalent-circuit models for split-ring resonators and complementary split-ring resonators coupled to planar transmission lines", *IEEE Trans. Microwave Theory Tech.*, vol. 53, no. 4, pp. 1451-1461, Apr. 2005.

[41] J. Garcia-Garcia, J. Bonache, I. Gil, F Martin, M Veazquez-Ahumada and J. Martel, "Miniaturized Microstrip and CPW filters using coupled metamaterial resonators", *IEEE Trans. Microwave Theory Tech.*, vol. 54, no. 6, pp. 2628-2635, June 2006.

[42] B Jokanovic, V Crnojevic-Bengin and O. Boric-Lubecke, "Miniature high selectivity filters using grounded spiral resonators", *Electronics Letters*, vol. 44, no. 17, Aug. 2008.

[43] F. Aznar, J. Garcia-Garcia, M. Gil, J. Bonache and F. Martin, "Strategies for the miniaturization of metamaterial resonators", *Microwave and Optical Technology Letters*, vol. 50, no. 5, May 2008, pp. 1263-1270.

[44] G. Sisó, J. Bonache, J. García-García and F. Martín, "Compact Rat-Race hybrid coupler implemented through artificial left-handed and right-handed lines", *IEEE MTT-S International Microwave Symposium*, pp. 25-28, 2007.

[45] V. Piatnitsa, D. Kholodnyak, P. Kapitanova, I. Fischuk, T. Tick, J. Jannti, H. Jantunen and I. Vendik, "Right/Left-handed transmission line LTCC directional couplers", *Proceedings of the 37th European Microwave Conference*, Munich, October 2007.

[46] R.H Geschke, B Jokanovic and P Meyer, "Compact Triple-Band Resonators Using Multiple Split-Ring Resonators", *European Microwave Week*, Rome, September 2009.

SAIEE Africa Research Journal

CALL FOR PAPERS – SPECIAL EDITION

METAMATERIALS: APPLICATION TO WIRELESS COMMUNICATIONS AND SENSORS

Topics of interest include:

- Analytical and numerical modelling of metamaterials
- Experimental techniques for characterisation of metamaterials
- Filters and microwave components based on metamaterials and metamaterial unit cells
- Antenna and absorber applications of metamaterials based on metamaterial concepts
- Metamaterials with extreme parameters such as epsilon near-zero and mu-near zero materials
- Planar metamaterial structures
- Electromagnetic bandgap structures and applications
- Tunable/reconfigurable/nonlinear metamaterial devices
- Educational aspects of metamaterials

Important dates:

Paper submission deadline:	28 February 2011
First response to authors:	29 April 2011
Revised papers due:	31 May 2011
Final notification:	8 July 2011
Publication date:	September 2011

SYSTEM IDENTIFICATION AND NEURAL NETWORK BASED PID CONTROL OF SERVO — HYDRAULIC VEHICLE SUSPENSION SYSTEM

O. A. Dahunsi *, **J. O. Pedro**† **and O. T. Nyandoro**‡

* *Sch. of Mechanical, Industrial and Aeronautical Engineering, University of the Witwatersrand, Private Bag 03, WITS2050, Johannesburg, South Africa. E-mail: Olurotimi.Dahunsi@students.wits.ac.za*

† *Sch. of Mechanical, Industrial and Aeronautical Engineering, University of the Witwatersrand, Private Bag 03, WITS2050, Johannesburg, South Africa. E-mail: Jimoh.Pedro@wits.ac.za*

‡ *Sch. of Electrical and information Engineering, University of the Witwatersrand, Private Bag 03, WITS2050, Johannesburg, South Africa. E-mail: Otis.Nyandoro@wits.ac.za*

Abstract: This paper presents the system identification and design of a neural network based Proportional, Integral and Derivative (PID) controller for a two degree of freedom (2DOF), quarter-car active suspension system. The controller design consists of a PID controller in a feedback loop and a neural network feedforward controller for the suspension travel to improve the vehicle ride comfort and handling quality. Nonlinear dynamics of the servo-hydraulic actuator is incorporated in the suspension model. A SISO neural network (NN) model was developed using the input-output data set obtained from the mathematical model simulation. Levenberg-Marquardt algorithm was used to train the NN model. The NN model achieved fitness values of 99.98%, 99.98% and 99.96% for sigmoidnet, wavenet and neuralnet neural network structures respectively. The proposed controller was compared with a constant gain PID controller in a suspension travel setpoint tracking in the presence of a deterministic road disturbance. The NN-based PID controller showed better performances in terms of rise times and overshoots.

Key words: Active vehicle suspension, PID, Neural network feedforward control, Servo-hydraulic actuator, Quarter-car model

1. INTRODUCTION

The design of vehicle suspension is a multidisciplinary challenge that requires compromise between complex and conflicting objectives in the face of disturbance inputs. These objectives includes: good ride comfort, good road handling, and good road holding qualities within an acceptable suspension travel range [1–3]. It is difficult to simultaneously satisfy all the design requirements for active vehicle suspension system (AVSS). Hence, a trade-off becomes necessary. Suspension travel is one of the readily measurable signal that makes the AVSS design and analysis realistic, especially within a feedback structure [4, 5].

AVSS control problem is a disturbance rejection problem, where the road roughness profile constitutes the external disturbance [3, 6]. Passive vehicle suspension remains the most popular choice for vibrations attenuation because of its simplicity and low cost. However, AVSS is the most feasible option due to its better system static stability and performance at low frequencies [3].

Numerous papers have highlighted the relative merits of semi and fully active systems [7–10]. Hrovat [6] gives a survey of applications of optimal control techniques for different types of car models, such as quarter-car, half-car, and full-car. Most of the numerical and experimental results failed to highlight the accompanying AVSS design challenges like measurement and actuator dynamic complications or the varying operating conditions of the vehicle [3, 11, 13, 14].

Controller designs based on complex multi-objective combinations like in [5] demonstrated good performance and robustness prospects. However, it is required that all the state variables be measured. This can result in a difficult to solve non-convex optimization problem.

AVSS controller designs based on linear parameter varying (LPV) control approach have been extensively applied to nonlinear models with considerations for actuator dynamics [15, 16]. However, LPV theory can only handle measurable and bounded nonlinearities [17]. LPV design is also one of the fixed-gain strategies that are designed to be optimal for nominal parameter set and specific operating condition.

The PID control is a generic control loop feedback mechanism, that remains the most industrially applied controller because of its simple structure, and the success of the Ziegler-Nichols tuning algorithms [18, 19]. Moreover, despite the straight forward Ziegler-Nichols tuning method, fine tuning of the constant gains is often done intuitively.

Copyright ©2010 SACAM: This is an extended version of of the paper presented at the 7th South African Conference on Computational and Applied Mechanics (SACAM10), 10 - 13 January, 2010, University of Pretoria, Pretoria, South Africa.

Previous works [11, 12] have shown that PID control possesses good prospects in terms of performance despite its disadvantages in terms of robustness, linearity and high loop gains [22–25]. This motivates for the augmentation of the PID controllers with genetic algorithm (GA) and fuzzy logic [26, 27]. The use of several evolutionary algorithms (EA) like the GA, particle swarm optimization (PSO) and differential evolution (DE) to obtain optimum PID gains has been reported in [19].

PID controller is used in this work in two forms; firstly, as a benchmark to evaluate the performance of the neural network based PID feedforward controller (PIDNN) designed for the AVSS. Secondly, as PID based controller with an overlay of NN inverse model in the feedforward mode.

It is customary in control design to use feedback as a means to stabilize unstable systems and to cut down the influence of disturbance inputs and model innacuracies. Feedforward control is known to enhance reference tracking in control designs. Control designs where feedback is used for reference tracking are usually sensitive to noise especially in systems lacking in robust properties [22].

Hagan and Demuth [28] and Cao et al. [29] highlighted various adaptive control properties of intelligent control techniques like NN, fuzzy logic, genetic algorithm and sliding mode control. NN have found wide applications in the field of control systems design because of their ability to approximate arbitrary nonlinear mapping and their highly parallel structure which allows parallel implementation, thus making it more fault-tolerant than the conventional schemes. NN also have the ability to learn and adapt on-line, and good application in multivariable systems [29–31].

The objective of system identification is to infer an approximate model of a dynamic system from its input - output data. It is desirable to seek a model with the closest representation possible especially when the system in question is nonlinear as is the case in this work. Application of NN and other intelligent techniques like fuzzy logic and genetic algorithm in system identification of nonlinear systems has been on the rise in the past two decades because of their capacity to overcome limitations encountered by the conventional methods [25, 32]

Neural network feedforward control is useful in optimizing many control problems especially in closed loop cases with stability properties. Steady-state feedforward control is not suitable for unstable systems since the control input is normally expected to be zero in steady-state systems [22].

This work aims to improve the reference tracking of the PID controller designed for the AVSS with a NN inverse model overlay in the feedforward mode. The achievement of good reference tracking through the use of feedback is usually accompanied by high sensitivity to noise. Thus in a situation where good controller performance has been achieved using feedback control, it is desirable to provide a guarantee for reduced sensitivity to noise through the addition of a suitable control technique in the feedforward mode [22].

The paper is organised as follows: The 2DOF, quarter-car AVSS model is described in Section 2. Section 3 describes the performance specifications, system identification process and controller design. Numerical simulation and discussion of results are presented in Section 4 before concluding the paper in Section 5.

2. SYSTEM MODELLING

2.1 Physical Modelling

The 2DOF, quarter-car AVSS is modelled as a dynamic system that consists of sprung mass m_s, and unsprung mass m_u. The masses are interconnected by nonlinear spring k_s, damper b_s and hydraulic actuator F, as shown in Figure 1, and k_t is the spring constant due to the compressibility of the pneumatic tyre. The vertical displacement of the car

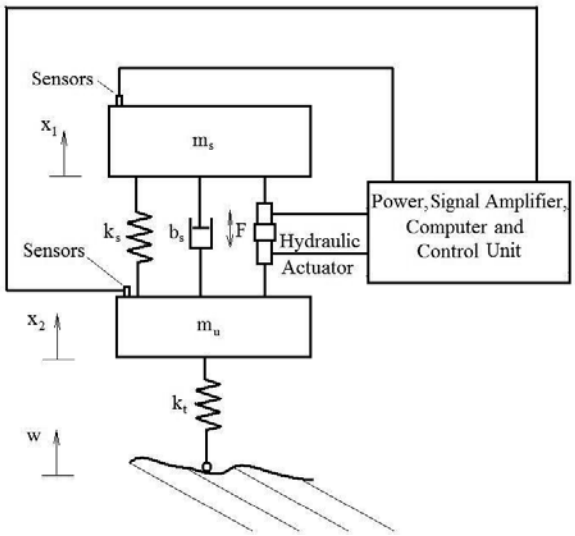

Figure 1: Simplified quarter car model

body, wheel and the road disturbance are represented by x_1, x_2 and w respectively. The hydraulic actuator force F is applied between the sprung and unsprung masses. The relative displacement between the vehicle body and the wheel $(x_2 - x_1)$, represents the suspension travel and the relative displacement between the wheel and the road $(x_2 - w)$, characterizes the road holding quality.

2.2 Mathematical Modelling

Application of Newton's law to the quarter car model shown in Figure 1 yields the governing equations in the state space form [15, 16, 33]:

$$\dot{\mathbf{x}} = \mathbf{f}(\mathbf{x}, \mathbf{w}) + \mathbf{g}(\mathbf{x})\mathbf{u}; \tag{1}$$

$$y = h(x) = y_1 = x_2 - x_1 \tag{2}$$

where:

$$\mathbf{f}(\mathbf{x},\mathbf{w}) = \left[\begin{array}{cccccc} f_1 & f_2 & f_3 & f_4 & f_5 & f_6 \end{array}\right]^{\mathbf{T}}, \tag{3}$$

$$\mathbf{g}(\mathbf{x}) = \left[\begin{array}{cccccc} 0 & 0 & 0 & 0 & 0 & \frac{1}{\tau} \end{array}\right]^{\mathbf{T}} \tag{4}$$

The state vector is

$$\mathbf{x} = \left[\begin{array}{cccccc} x_1 & x_2 & x_3 & x_4 & x_5 & x_6 \end{array}\right]^{\mathbf{T}} \tag{5}$$

and the control input is u.

$$f_1 = x_3 \tag{6}$$

$$f_2 = x_4 \tag{7}$$

$$\begin{aligned} f_3 = \frac{1}{m_s}\Big\{ & k_s^l(x_2-x_1) + k_s^{nl}(x_2-x_1)^3 + b_s^l(x_4-x_3) \\ & -b_s^{sym}|x_4-x_3| + b_s^{nl}\sqrt{|x_4-x_3|}sgn(x_4-x_3) \\ & -Ax_5\Big\} \end{aligned} \tag{8}$$

$$\begin{aligned} f_4 = \frac{1}{m_u}\Big\{ & -k_s^l(x_2-x_1) - k_s^{nl}(x_2-x_1)^3 - b_s^l(x_4-x_3) \\ & +b_s^{sym}|x_4-x_3| - b_s^{nl}\sqrt{|x_4-x_3|}sgn(x_4-x_3) \\ & -k_t(x_2-w) + Ax_5\Big\} \end{aligned} \tag{9}$$

$$f_5 = \gamma\Phi x_6 - \beta x_5 + \alpha A(x_3 - x_4) \tag{10}$$

$$f_6 = \frac{-x_6}{\tau} \tag{11}$$

where; $\Phi = \phi_1 + \phi_2$, $\phi_1 = sgn[P_s - sgn(x_6)x_5]$, $\phi_2 = \sqrt{|P_s - sgn(x_6)x_5|}$, $\alpha = \frac{4\beta_e}{V_t}$, $\beta = \alpha C_{tp}$, and $\gamma = C_d S\sqrt{\frac{1}{\rho}}$. A is the area of the piston, x_3 and x_4 are the vertical velocities of the sprung and unsprung masses respectively, x_5 is the pressure drop across the piston, x_6 is the servo valve displacement, P_s is the supply pressure going into the cylinder and P_r is the return pressure going out of the cylinder. P_u is the oil pressure in the upper portion of the cylinder and P_l is the oil pressure in the lower portion of the cylinder. V_t is the total actuator volume, β_e is the effective bulk modulus of the system, Φ is the hydraulic load flow, C_{tp} is the total leakage coefficient of the piston, C_d is the discharge coefficient, S is the spool valve area gradient and ρ is the hydraulic fluid density.

The spring and damping forces have linear and nonlinear components. Spring constant k_s^l and damping coefficient b_s^l affects the spring force and damping force in the linear region. b_s^{sym} contributes an asymmetric characteristics to the overall behaviour of the damper. k_s^{nl} and b_s^{nl} are responsible for the nonlinear components of the spring and damper forces respectively.

Figure 2 illustrates the hydraulic actuator mounted in between the sprung and unsprung masses. Q_u and Q_l are the hydraulic fluid flow rates into the upper and the lower chambers of the hydraulic cylinder respectively.

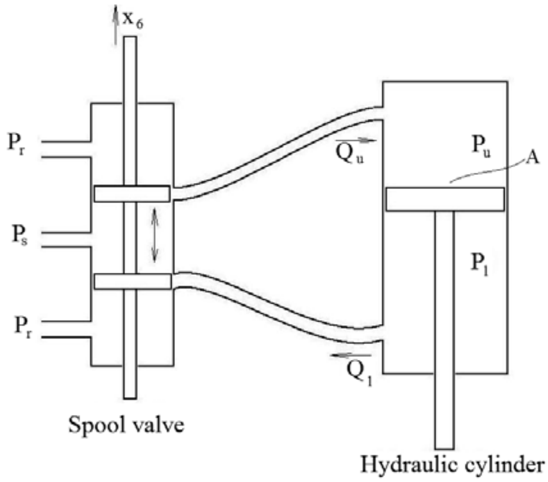

Figure 2: Schematic of the double acting hydraulic strut

The actuator is controlled by means of electro-hydraulic servo-valves in a three land four-way spool valve system. The maximum control input (voltage) of $10V$ was applied to the servo-valves to achieve a maximum suspension travel of $10cm$.

The deterministic road disturbance used in Equation 9 is given by:

$$w(t) = \begin{cases} \frac{a}{2}(1 - cos\frac{2\pi Vt}{\lambda}) & 1.25 \le t \le 1.5 \\ 0 & \text{otherwise} \end{cases} \tag{12}$$

where a is the bump height, V is the vehicle speed and λ is the half wavelength of the sinusoidal road undulation. Figure 3 shows the road disturbance profile.

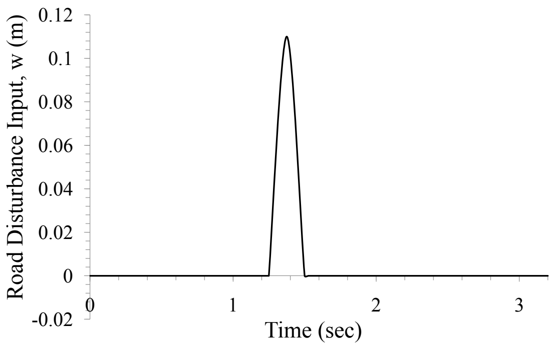

Figure 3: Road profile

The values of the system parameters used in the modelling are given in Table 1:

3. CONTROLLER DESIGN

The controller design is based on the indirect adaptive control approach, using PID feedback control that is complemented by feedforward generated by an inverse neural network model. The NN-based controller implementation requires the following two steps: system

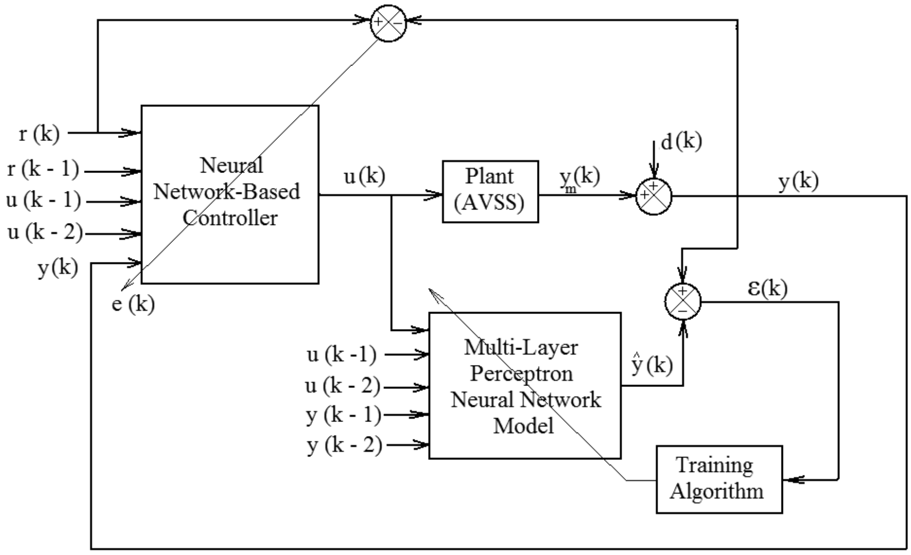

Figure 4: Architecture for Neural Network based System Identification and Control

Table 1: Parameters of the Quarter-Car Model [15, 16]

Parameters	Value
sprung mass (m_s)	290kg
unsprung mass (m_u)	40kg
suspension stiffness (k_s^l)	$2.35*10^4 N/m$,
suspension stiffness (k_s^{nl})	$2.35*10^6 N/m$
tyre stiffness (k_t)	$1.9*10^5 N/m$
suspension damping (b_s^l)	$700 Ns/m$
suspension damping (b_s^{nl})	$400 Ns/m$
suspension damping (b_s^{sym})	$400 Ns/m$
actuator parameter (α)	$4.515*10^{13}$
actuator parameter (β)	1
actuator parameter (γ)	$1.545*10^9$
piston area (A)	$3.35*10^{-4} m^2$
supply pressure (P_s)	$10,342,500 Pa$
time constant (τ)	$3.33*10^{-2} sec$
bump height (a)	$0.11 m$
vehicle speed (V)	$30 ms^{-1}$
disturbance half wavelength (λ)	$7.5 m$

identification and controller design.

In order to design a NN-based controller, it is essential to first obtain an accurate dynamic model, through system identification, as a representation of the actual system. Figure 4 shows the schematic architecture for system identification and controller design of the system, where $\hat{y}(k)$ is the identified model output, $d(k)$ is the disturbance signal, $\varepsilon(k) = y(k) - \hat{y}(k)$ the error signal, $y(k)$ is the controlled output, $u(k)$ is the control input, and $e(k) = r(k) - y(k)$.

The main goal of the controller is to track a generated desired suspension travel in the presence of the deterministic road disturbance (Equation 12). The controller should satisfy the following requirements:

1. Nominal stability: The closed loop should be nominally stable.
2. Good command following: The controller should be able to track a square wave reference trajectory with rise time not greater than $0.1 sec$, maximum overshoot not greater than 5% and without steady state error.
3. Disturbance rejection: The controller should demonstrate good low frequency disturbance attenuation.
4. Performance index: The controller should minimize the performance index given by:

$$J = \frac{1}{t_f}\int_0^{t_f}\left[\left(\frac{y(t)-y_{ref}(t)}{y_{max}}\right)^2 + \left(\frac{u(t)}{u_{max}}\right)^2\right] dt \tag{13}$$

   where t_f is the final time (which in this case is $5 sec$), y_{ref} is the desired suspension travel, y_{max} is the the maximum allowable value of the suspension travel (controlled output), and u_{max} is the maximum allowable value of the supply voltage (control input).

3.1 Nonlinear System Identification

System identification stage is a function approximation process where the dynamic model of the system is established based on observed input-output data. Feedforward, multilayer perceptron (MLP), error back propagation neural network is used here for the system identification. This is due to its simplicity and ability to learn nonlinear relations from a set of input-output data [22].

Training inputs are supplied to the input layer of the network in a forward sweep such that the output of each element is computed layer by layer. Backpropagation training is a process of training the network with the input and target vectors until it can associate input vectors with appropriate output vectors [34].

In this work, the suitability of the neural network in developing dynamic models that is representative of the actual nonlinear plants based on the interactions between the inputs and outputs is exploited. The identification process consists of the four steps shown in Figure 5: experimentation, model structure selection, model estimation and model validation [22]. Control design stage comes after the system identification, here the NN plant model is used to design the controller.

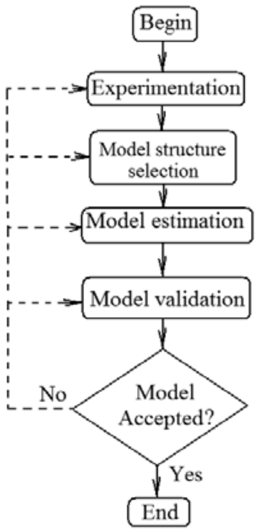

Figure 5: Flowchart form of system modelling procedure

The objective of the identification process is to minimize the error signal $\varepsilon(k) = y(k) - \hat{y}(k)$, where k = 1,......,N (see Figure 6). The NN parameters in the identification model are adjusted in an increasing manner until the training data satisfies the desired performance criteria, which in this case is the sum of the mean square error (MSE) [25,34,35]:

$$MSE = \gamma \frac{1}{N} \sum_{k=1}^{N} [y(k) - \hat{y}(k)]^2 = \gamma \frac{1}{N} \sum_{k=1}^{N} \varepsilon^2(k) \qquad (14)$$

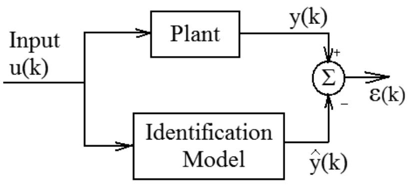

Figure 6: Basic system identification structure

where γ is the performance ratio. The choice of the performance ratio must be considered with caution since it represents the relative weight between the mean square errors and the mean square network parameters (that is, weights and biases). The choice of γ may influence the smoothness of the network response. The sampling time is chosen in accordance with the fastest dynamics of the system [22, 33].

Experimentation:

The AVSS is identified from a set of input-output data pairs collected from numerical experiments. These are given in form of the AVSS model Equations (1) - (6) simulations and collected in the form:

$$Z^N = f[u(k), y(k)]; \quad k = 1, ..., N \qquad (15)$$

where Z^N is the input-output data set, $u(k)$ is the input signal, $y(k)$ is the output signal, k is the sampling instant, and N is the total number of samples. The input-output data was collected using the structure illustrated by Figure 7:

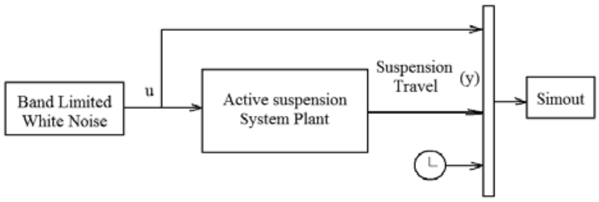

Figure 7: Structure input-output data collection

The AVSS plant model identification was conducted using a 20,000 input-output data pairs - divided into two equal parts for training and validation as shown in Figures 8 and 9. A non-saturating "band-limited white noise" random input was used to excite the AVSS plant in its operating range, $u(k) \in [-10V, +10V]$. The sampling interval of $0.001 sec$ was chosen in accordance with the fastest dynamic of the system [22, 33].

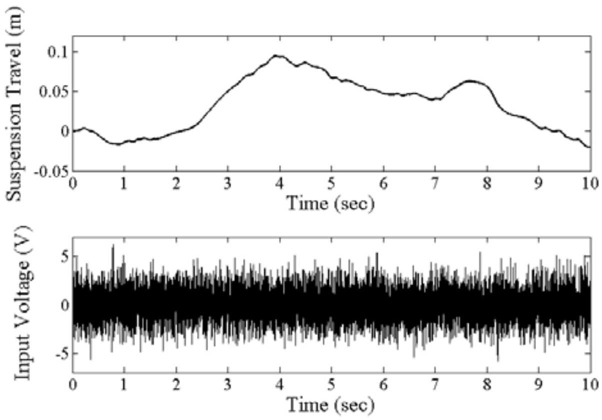

Figure 8: Estimation (training) data set

Model Structure Selection:

The Neural Network AutoRegressive eXogenous inputs (NNARX) model has been proven to readily represent any nonlinear, discrete, time-invariant system. It is preferable

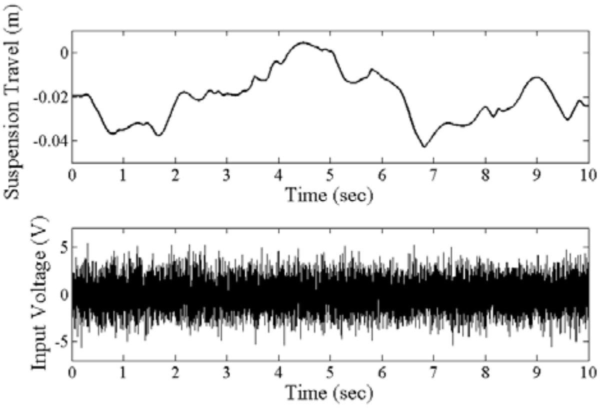

Figure 9: Validation data set

when the system order is high, however, increasing its order could affect some dynamic characteristics like stability. It is also simpler, non-recursive (unlike nonlinear models based output error (OE) and Auto Regressive Moving Average with eXogenous inputs (ARMAX), wherein future inputs depend on present and future outputs) and more stable since it requires no feedback [20,22,36]. The general structure of the NNARX is shown in Figures 10 and 11.

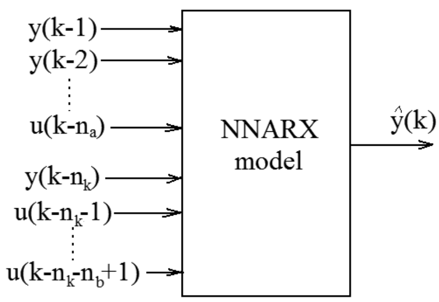

Figure 10: NNARX model structure

The AVSS nonlinear system can be represented by NNARX model structure for a finite number of past inputs $u(k)$ and outputs $y(k)$ [20,25,37,38]:

$$y(k) = f[\phi(k), \theta] + \vartheta(k) \tag{16}$$

As a result of the numerical experiment and training, the network implements an estimation of the nonlinear transformation, $\hat{f}(*)$ which leads to the predicted output. The one-step ahead prediction (1-SAP) based on the identification structure is given by:

$$\hat{y}(k) = f[\phi(k), \theta] \tag{17}$$

and the regression vector is

$$\begin{aligned}\phi(k) \quad &= \quad [y(k-1), y(k-2), \ldots, y(k-n_a), u(k-n_k), \\ &\quad\quad u(k-n_k-1), \ldots, u(k-n_k-n_b+1)\end{aligned}$$

where f is the nonlinear function that is realized by the

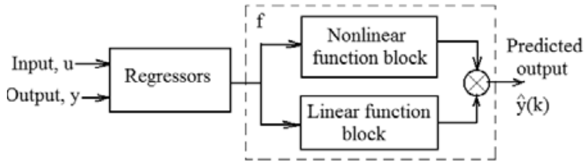

Figure 11: Neural network nonlinear ARX Structure

neural network model, $\phi(k)$ represents the regressors, vector θ contains the adjustable weights, $\vartheta(k)$ represents the model residual, n_k delay from input to the output in terms of number of samples, and n_a and n_b make up the order of the system which is the number of output and inputs used to predict the new output. Lipschitz algorithm was used to the determine the system lag (see Figures 12 and 13). The figures present the plot of the order index based on the evaluated Lipschitz quotients for the input - output pair combinations against the lag space (number of past inputs and outputs) ranging from 1 to 10.

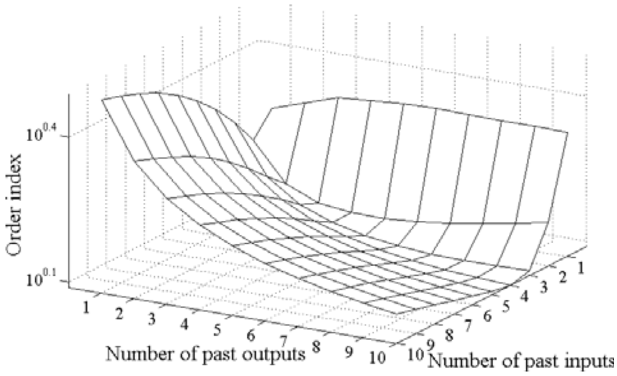

Figure 12: Model order determination by lag-space method

Figure 13 shows that the slope of the graph decreases when the model order is ≥ 2, thus defining the ”knee point” of the curve. This leads to the choice of two as the number of past inputs and outputs respectively; and the number of neurons in the hidden layer becomes five since the time delay is one [22,25]. The choice of a model order higher than two may result in data overfitting with lower MSE.

Model Estimation:

The neural network structures are selected for use in the network training of the model. Simplicity of the NN structure and computational ease are two guiding factors considered in the model estimation process. Thus a feedforward multilayer perceptron neural network (MLPNN) structure that contains: an input layer, a hidden layer and an output layer shown in Figure 14 was developed. The parameters for training of the neural network model are listed in Table 2.

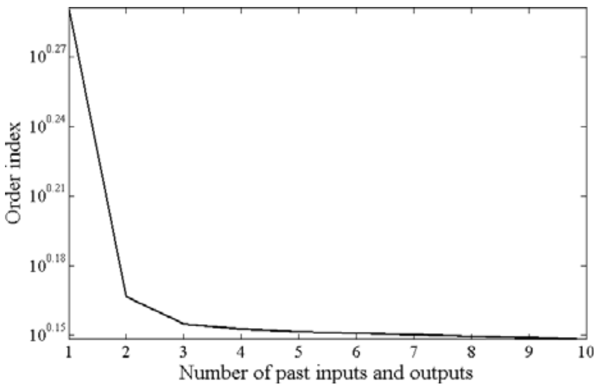

Figure 13: Two dimensional view of the order of index versus lag - space

Levenberg-Marquardt minimization algorithm was used to train the network due to its rapid convergence and robustness. The input layer contains two neurons and a bias, the hidden layer contains five neurons with tangent hyperbolic activation function:

$$f(x) = tanh(x) = \frac{e^x - e^{-x}}{e^x + e^{-x}} \tag{18}$$

while the output layer contains one neuron with linear activation function [21, 22, 39].

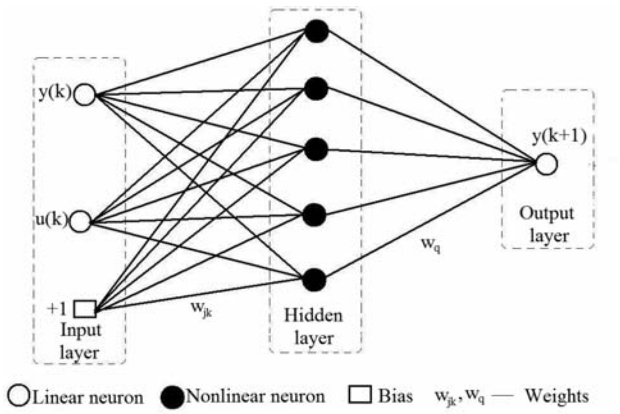

Figure 14: Neural network layer structure

The choice of Levenberg-Marquardt training algorithm is motivated by the results shown in Table 3. It has the least mean square error (MSE) using the maximum number of available epochs (300). Levenberg-Marquardt training algorithm is also preferred to the other algorithms because it improves over time relative to the other algorithms and it is a compromise between the gradient descent and Newton optimization methods [22, 34, 40].

Model Validation:

The performance of the trained network as based on the validation data is shown in Figure 15 where the quality of the identification is indicated by the mean square error, which is of the order of 10^{-11}.

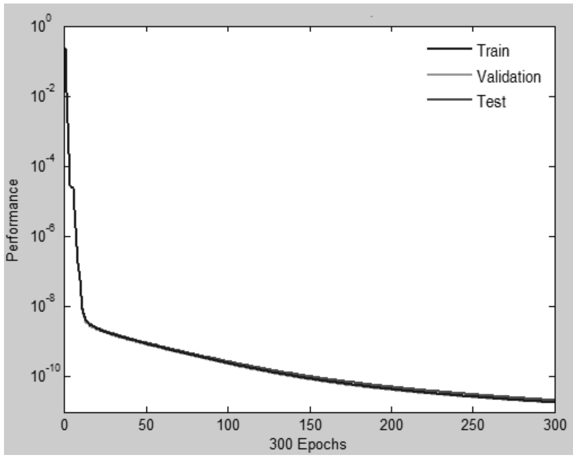

Figure 15: Neural network training performance

Figure 16 presents the fitness analysis of three one-step ahead predictions for sigmoidnet, wavenet and neuralnet structures to the validation data. The fitness values for each structures were 99.98%, 99.98% and 99.96% respectively.

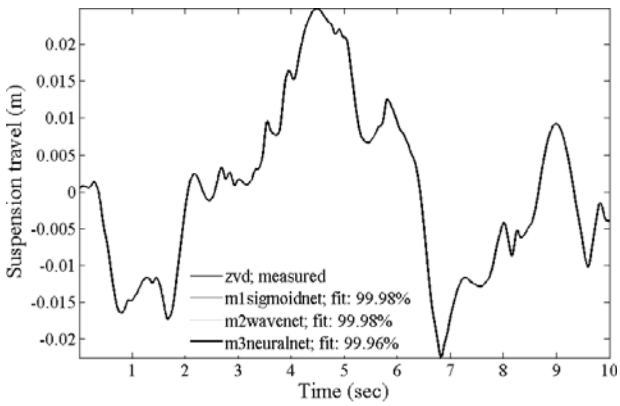

Figure 16: Fitness analysis for one-step ahead predictions based on sigmoidnet, wavenet and neuralnet structures

In Figure 17 the residuals were found to be of the order of 10^{-8}. Figure 18 shows a relatively steady auto-correlation trend of the residuals and about 90% of the points for cross-correlation between the input signal and the residuals of the output (suspension travel) falls within the 95% confidence interval. The validity of the model is further demonstrated by the low mean square error value $(1.84492 * 10^{-11})$ in Figure 15, high percentage fitness values in Figure 16 and low order of the residuals in Figure 17.

Table 2: Parameters for the Neural Network Model

Parameters	Value	Parameters	Value
Total number of samples	500 (control)	Total sampling time	5sec
Number of training epochs	300	Number of iterations	10,000
		Time delay	1
Training algorithm	Levenberg-Marquardt algorithm	Number of hidden layer neurons	5
Number of layers	2	sampling time, T_s	0.001sec
Number of past outputs	2	Number past inputs	2

Table 3: Performance of Neural Network Training Functions

	Algorithm	Number of Epochs used out of 300	Mean Square Error
1	BFGS quasi-Newton backpropagation	75	$3.15857 * 10^{-6}$
2	Powell-Beale conjugate gradient backpropagation	13	$1.46828 * 10^{-4}$
3	Fletcher-Powell conjugate gradient backpropagation	188	$4.95962 * 10^{-6}$
4	Polak-Ribiere conjugate gradient backpropagation	68	$7.3317 * 10^{-6}$
5	Gradient descent backpropagation	300	$9.50216 * 10^{-3}$
6	Gradient descent with momentum and adaptive backpropagation	300	$1.00666 * 10^{-2}$
7	Gradient descent with adaptive learning backpropagation	243	$5.07354 * 10^{-4}$
8	Gradient descent with momentum and adaptive backpropagation	159	$1.19449 * 10^{-4}$
9	Levenberg-Marquardt backpropagation	300	$1.84492 * 10^{-11}$
10	One step secant backpropagation	90	$5.81278 * 10^{-6}$
11	Resilient backpropagation	300	$7.87337 * 10^{-6}$
12	Scaled conjugate gradient backpropagation	52	$1.4651 * 10^{-5}$

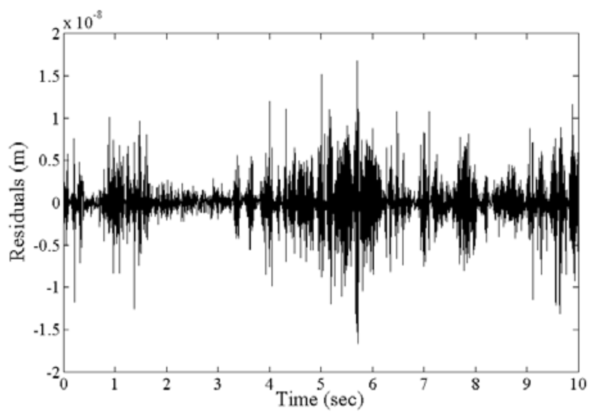

Figure 17: Model residuals

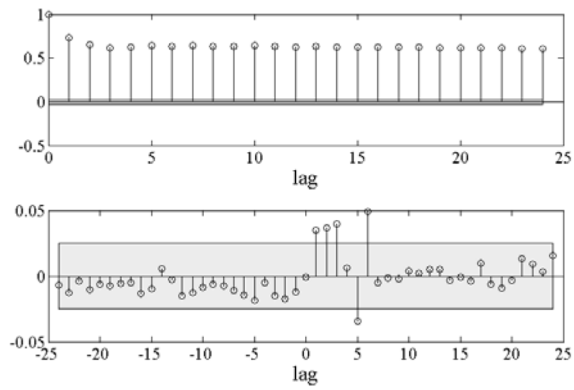

Figure 18: Auto and Cross Correlation Analysis

3.2 PID Control and Tuning

The structure of the PID controller is given as [22,42]:

$$U(s) = \left(K_p \frac{1+T_i s}{T_i s} \frac{1+T_d s}{1+\alpha T_d s}\right) E(s) \tag{19}$$

where $E(s) = Y_{ref}(s) - Y(s)$ is the error signal, $Y_{ref}(s)$ is the reference signal, $Y(s)$ is the actual output signal, $U(s)$ is the plant input signal, K_p is the proportional gain, T_d is the derivative time constant, T_i is the integral time constant and α is the lag factor in the derivative component of the PID controller.

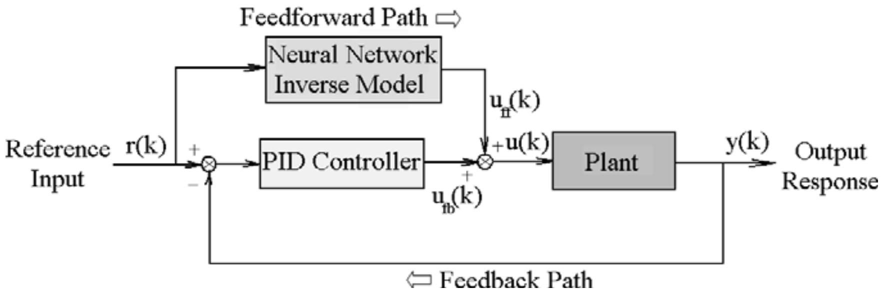

Figure 19: PID Feedback Scheme being Optimised with a Neural Network Inverse Model

Table 4: PIDNN and PID tuning parameters used

Parameters	PIDNN Tuning Values	PID Tuning Values
Proportional gain, K_p	6.5	3.0
Integral time, T_i	0.0238	0.0667
Derivative time, T_d	0.4041	0.04035
Lag factor, α	0.0147	0.047

Ziegler-Nichols tuning rule is used with a decay ratio of 0.25 to obtain the PID controller gains. PID controllers are known to often generate high control inputs which can lead to saturation. Thus, efforts were made during tuning to ensure that the control input was within the stipulated range. The tuning parameters are presented in Table 4.

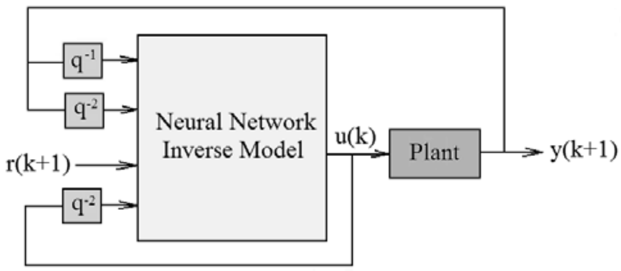

Figure 20: Direct Inverse Control

3.3 *Neural Network Based Feedforward Control*

The control structure in Figure 19 presents an arrangement for a PID control feedback overlaid with a neural network (PIDNN) inverse model. The essence of the neural network inverse model is to optimise the performance of the PID controller based on the principle of additive feedforward. This method is one of the direct control design of the neural network based control. It is sometimes useful in regulation problems where the reference attains constant levels for longer periods of time, it helps in speeding up the tracking of set points changes [22].

The inverse model is illustrated in Figure 20. The training of a network as an inverse of a system requires the application of the system identification procedure illustrated by Figure 5 but it is done off-line.
Moreover, the difference of the inverse NN model is in the choice of the regressors and network output. The inverse model is here applied to AVSS plant by inserting the desired output, reference $r(k+1)$, instead of the system output $y(k+1)$, which is an unknown value, at the input point of the inverse model, this training is implemented in the form shown in Equation 21. If the AVSS is described by [22,41]:

$$y(k+1) = g[y(k),\dots,y(k-n_a+1,u(k),\dots,u(k-n_b)] \tag{20}$$

then the desired network is the one that isolates the latest control input, $u(k)$ given by

$$\begin{aligned}\hat{u}(k) &= \hat{g}^{-1}[r(k+1),y(k),\dots,y(k-n_a+1,\\ &\quad u(k),\dots,u(k-n_b)]\end{aligned} \tag{21}$$

the network is then trained to minimize the criterion

$$J(\theta,Z^N) = \frac{1}{2N}\sum_{k=1}^{N}[u(k)-\hat{u}(k|\theta)]^2 \tag{22}$$

The system outputs are substituted with the corresponding feedforward component of the control input given by

$$\begin{aligned}u_{ff}(k) &= \hat{g}[r(k-1),\dots,r(k-n_a+1,\\ &\quad u_{ff}(k-1),\dots,u_{ff}(k-n_b)]\end{aligned} \tag{23}$$

this can then be used to drive the system output at $k+1$ to reference $r(k+1)$ as shown in Figures 4 and 20.

The network is trained by invoking Levenberg-Marquardt training algorithm (system identification). This was done off-line by minimizing the criterion $J(\theta,Z^N)$ where θ specifies the weights of the network. Ziegler-Nichol's tuning rule, with a decay ratio of 0.25, is used to obtain the tuning parameters for the PIDNN as presented in Table 4.

4. RESULTS AND DISCUSSION

The physical model which is represented by Figure 1 has been modelled mathematically in the state-space form given by Equations 1-11. Numerical experimentation based on the mathematical model yielded a NN model of the plant that was used in the controller design.

The PIDNN and PID controller were applied to an AVSS nonlinear model with actuation force generated by an electro-hydraulic actuator. A variable but preset control input in the form of voltage (which was $\leq$ 10V) was supplied to the servo-valve to generate the actuation force at the piston. The control problem given by Equation 1 is to obtain a control input, $u(t)$ that follows a reference trajectory $y(t)$ while minimizing the performance criterion (Equation 13). Meanwhile, the reciprocals of the squared values of y_{max} and u_{max} gives the values of the weighting factors that was used in the computation of the performance index.

The identification and control processes were implemented in MATLAB using the MATLAB system identification toolbox and neural network based control system design (NNCNTRL20) toolboxes. The parameters used for the simulations are given in Tables 1, 2 and 4.

Figures 21 and 22 present the command tracking of both controllers.The PIDNN tracking is characterized by the presence of marginal steady state error and overshoots that diminished with time, but the trajectory tracking of the PID appear better though its overshoots at the points of transition is a regular feature. The maximum overshoot measured for the PIDNN is just marginally greater than overshoot in the PID control, but the maximum overshoots for both controller exceed the specified values.

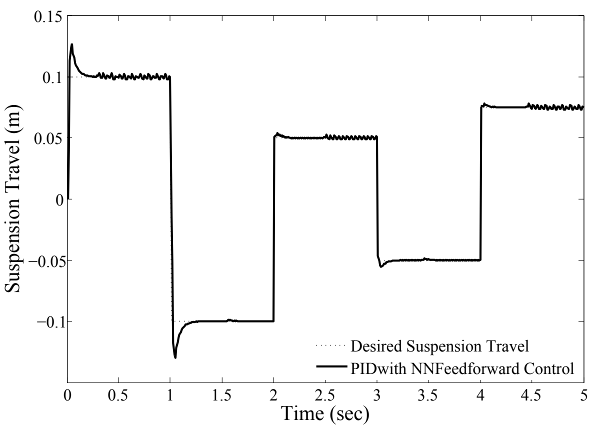

Figure 21: Suspension travel reference tracking using the NN based PID controller

Both controllers have rise times that are below the specified value for design but the rise time for PIDNN is 0.004*sec* lower than that for the PID controller. The PIDNN controller could not also reach the zero steady state error like the PID because of the oscilations that

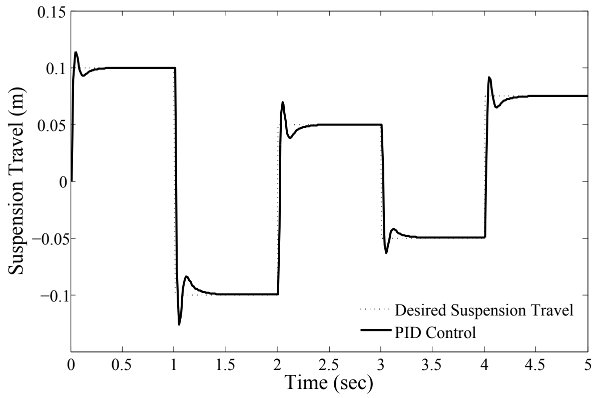

Figure 22: Suspension travel reference tracking using the PID controller

occur just before the transition point.

Figures 23 and 24 show the cost of achieving the performance of the PIDNN controller summarised in Table 5 in terms of the supplied voltage to the servo valve of the actuator as control input. The supply voltage to the PIDNN was characterized by continuous chattering and it exceeded the required supply voltage value in four instances. The maximum range of the supply voltage to the PID controller is $-4.2V - 3.3V$. The PID supply voltage is also characterized by spikes at the transition points.

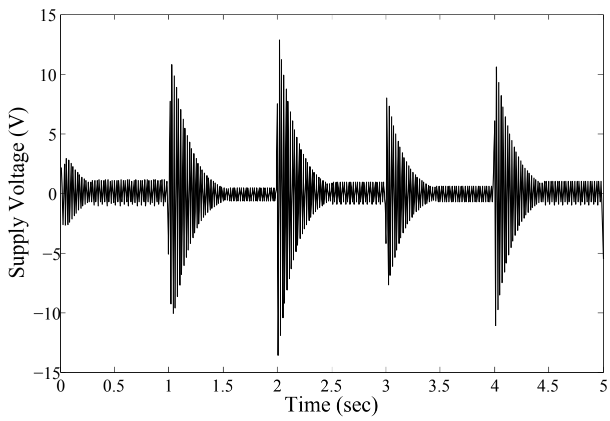

Figure 23: NN based PID control input

Complete minimization of the performance criterion could not be achieved by both controllers but the performance index of the PID is twice better than the performance index of the PIDNN controller. This performance criterion has put into consideration the sum of square of the weighted controlled output error and the control input.

Considering the values for all the performance evaluation parameters listed in Table 5, the overall superior performance of the PID controller is evident but from Figure 25, the performances of the PID controller at the transitional points are not as physically realisable as the PIDNN. While the PIDNN gradually returns to zero, the PID controller shoots to higher performance index at these

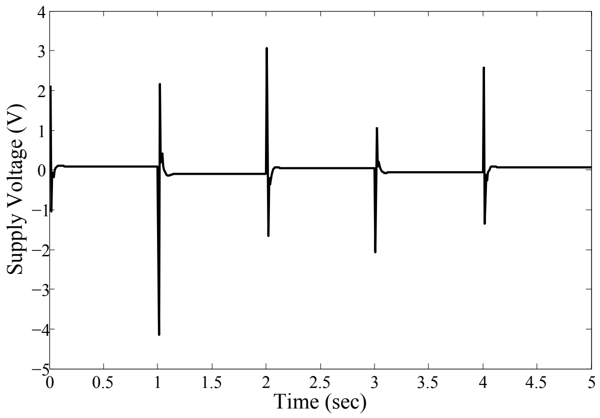

Figure 24: PID control input

points and returns to zero immediately.

Table 5: Evaluation of the controller performances

Performance parameters	Specified values	PIDNN	PID
Maximum overshoot	$\leq 5\%$	27.7%	26.1%
Rise time, *sec*	$\leq 0.1\%$	0.014	0.018
Steady state error	0%	4%	0%
Control input, *V*	± 10	136%	42%
Performance index, *J*	0	0.057	0.025

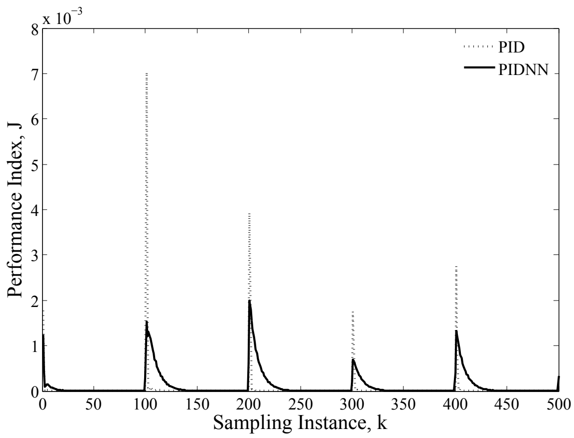

Figure 25: Comparison of Performance Indices at all the Sampling Instances

5. CONCLUSION

A PID controller with a neural network feedforward control has been designed for a nonlinear AVSS. The system identification process to obtain an inverse NN model for the controller design was achieved at an average fitness value of 99.98% and prediction error with order of 10^{-8}.

Both controllers were able to track the reference well though with overshoots and both controllers had rise time values that were less than the required. The supply voltage to the PIDNN exceeded the limits at four instance while the PID controller was always lower than the supply voltage limit by at least 50%.

The performance index for the PID controller was twice lower than the index for the PIDNN but examination of the performance indices at each sampling instances showed that, although the PID controller had better performance than the PIDNN, it is less physically realisable than the PIDNN control.

The choice of PIDNN over the conventional PID control is due to drawbacks like the nonlinear nature of AVSS and its susceptibility to parameter and disturbance variation, often PID controller design fail to guarantee robustness and model uncertainty.

REFERENCES

[1] H. Du and N. Zhang: "H_∞ Control of Active Vehicle Suspensions with Actuator Time Delay", *Journal of Sound and Vibration*, Vol. 301, No. 1-2, pp. 236-252, March 2007.

[2] M. S. Kumar and S. Vijayarangan: "Analytical and Experimental Studies on Active Suspension System of Light Passenger Vehicle to Improve Ride Comfort", *Mechanika*, Vol. 65, No. 3, pp. 34-41, June 2007.

[3] J. O. Pedro: "H_2 - LQG/LTR Controller Design for Active Suspension Systems",*R and D Journal of the South African Institution of Mechanical Engineering*, Vol. 23, No. 2, pp. 32-41, November 2007.

[4] B. Gao, D. G. Tilley, R. A. Williams, A. Bean and J. Donahue: "Control of Hydropneumatic Active Suspesion based a nonlinear Quarter-Car Model",*Proceedings of the Institute of Mechanical Engineers, Part I*, Vol. 220, No. 1, pp. 75-81, January 2006.

[5] H. Du and N. Zhang: "Designing H_∞/GH_2 Static - Output Feedback Controller for Vehicle Suspensions Using Linear Matrix Inequalities and Genetic Algorithms", *Vehicle Systems Dynamics*, Vol. 46, No. 5, pp. 385-412, May 2008.

[6] D. Hrovat: "Survey of Advanced Suspension Developments and Related Optimal Control Applications", *Automatica*, Vol. 33, No. 10, pp. 1781-1817, October 1997.

[7] M. K. Ghosh and R. Dinavahi: "Vibration Analysis of a Vehicle System Supported on a Damper-Controlled Variable-Spring-Stiffness Suspension", *Proceedings of the Institute of Mechanical Engineers, Part D*, Vol. 219, No. 5, pp. 607-619, May 2005.

[8] I. Ballo: "Comparison of the Properties of an Active and Semi-Active Suspension", *Vehicle System Dynamics*, Vol. 45, No. 11, pp. 1065-1073, November 2007.

[9] J. Renn and T. Wu: “Modelling and Control of a new $\frac{1}{4}T$ Servo-Hydraulic Vehicle Active Suspension System”, *Journal of Marine Science and Technology*, Vol. 15, No. 3, pp. 265-272, September 2007.

[10] M. Biglarbegian, W. Melek and F. Golnaraghi: “A Novel Neuro-Fuzzy Controller to Enhance the Performance of Vehicle Semi-Active Suspension Systems”, *Vehicle System Dynamics*, Vol. 46, No. 8, pp. 691-711, August 2008.

[11] O. A. Dahunsi, J. O. Pedro and O. T. Nyandoro: “Neural Network-Based Model Predictive Control of a Servo-Hydraulic Vehicle Suspension System”, *Proceedings of the 2009 IEEE Africon*, Nairobi, Kenya, September 2009.

[12] O. A. Dahunsi, J. O. Pedro and O. T. Nyandoro: “Neural Network-Based PID Control of a Servo-Hydraulic Vehicle Suspension System”, *Proceedings of the Seventh South African Conference on Computational and Applied Mechanics (SACAM10)*, University of Pretoria, South Africa, January 2010.

[13] S. Chantranuwathana and H. Peng: “Adaptive Robust Force Control for Vehicle Active Suspension”, *International Journal of Adaptive Control and Signal Processing*, Vol. 18, No. 2, pp. 83 - 102, March 2004.

[14] X. Shen and H. Peng: “Analysis of Active Suspension Systems with Hydraulic Actuators”, *Proceedings of the 2003 IAVSD Conference*, Atsuigi, Japan, pp. 1-10, August 2003.

[15] I. Fiahlo and G. J. Balas: “Road Adaptive Active Suspension using Linear Parameter-Varying Gain-Scheduling”, *IEEE Transactions on Control Systems Technology*, Vol. 10, No. 1, pp. 43-54, January 2002.

[16] P. Gaspar, I. Szaszi and J. Bokor: “Active Suspension Design Using Linear Parameter Varying Control”, *International Journal of Autonomous Systems (IJVAS)*, Vol.1, No. 2, pp. 206 - 221, June 2003.

[17] C. Poussot-Vassal, O. Sename, L. Dugard, P. Gaspar, Z. Szabo and J. Bokor: “Multi-objective qLPV H_∞/H_2 Control of a Half Vehicle”, *Proceedings of the 10th MINI Conference on Vehicle System Dynamics, Identification and Anomalies*, Budapest, Hungary, November 2006.

[18] J. G. Juang, M. T. Huang and W. K. Liu: “PID Control Using Presearched Genetic Algorithms for a MIMO System”, *IEEE Transactions on Systems, Man, and Cybernetics-part C:Applications and Reviews*, Vol. 38, No. 5, pp. 716 - 727, September 2008.

[19] M. W. Iruthayarajan and S. Baskar: “Evolutionary Algorithms Based Design of Multivariable PID Controller”, *Expert Systems with Applications*, Vol. 36, No. 5, pp. 9159 - 9167, July 2009.

[20] J. D. Bomberger and D. E. Seborg: “Determination of Model Order for NARX Models Directly from Input - Output Data”, *Journal of Process Control*, Vol. 8, No. 5, pp. 459 - 468, October 2009.

[21] M. Norgaard: “Neural Networks Based Control System Design”, *Tech.Report 00-E-892*, Department of Automation, Technical University of Denmark, 2000.

[22] M. Norgaard, O. Ravn, N. K. Poulsen and L. K. Hansen: “Neural Networks for Modelling and Control of Dynamic Systems: A Practitioner’s Handbook”, *Springer*, Boston, MA, 2000.

[23] Z. Gao: “From Linear to nonlinear Control Means: A Practical Progression”, *ISA Transactions*, Vol. 41, No. 2, pp. 177-189, April 2002.

[24] A. Herreros, E. Baeyens and J. R. Peran: “Design of PID - type Controllers Using Multiobjective Genetic Algorithms”, *ISA Transactions*, Vol. 41, No. 4, pp. 457 - 472, October 2002.

[25] N. Kishor, R. P. Saini and S. P. Singh: “Small Hydro Power Plant Identification Using NNARX Structure”, *Neural Computing and Applications*, Vol. 14, No. 3, pp. 212 - 222, September 2005.

[26] J. Z. Feng, J. Li and F. Yu: “GA-Based PID and Fuzzy Logic Control for Active Vehicle Suspension System”, *International Journal of Automotive Technology*, Vol. 4, No. 4, pp. 181- 191, December 2003.

[27] Y. Kuo and T. S. Li: “GA-Based Fuzzy PI/PD Controller for Automotive Active Suspension System”, *IEEE Transactions on Industrial Electronics*, Vol. 46, No. 6, pp. 1051 - 1056, December 1999.

[28] M. T. Hagan and H. B. Demuth: “Neural Networks for Control”, *American Control Conference*, Invited Tutorial for American Control Conference 1999, pp. 1642 - 1656, San Diego, USA June 1999.

[29] J. Cao, H. Liu, P. Li and D. Brown: “State of the Art in Vehicle Active Suspension Adaptive Control Systems based on Intelligent Methodologies”, *IEEE Transactions of Intelligent Transportation Systems*, Vol. 9, No. 3, pp. 392 - 405, September 2008.

[30] Y. Jin and D. J. Yu: “Adaptive Neuron Control Using an Integrated Error Approach with Application to Active Suspensions”, *International Journal of Automotive Technology*, Vol. 9, No. 3, pp. 329 - 335, June 2008.

[31] I. Eski and S. Yildrim: “Vibration Control of Vehicle Active Suspension System Using a New Robust Neural Network Control System”, *Simulation Modelling Practice and Theory*, Vol. 17, No. 5, pp. 778 - 793, May 2009.

[32] K. Valarmathi, D. Devaraj and T. K. Radhakrishnan: "Intelligent Techniques for System Identification and Controller Tuning in pH Process", *Brazilian Journal of Chemical Engineering*, Vol. 26, No. 1, pp. 99 - 111, January - March 2009.

[33] M. Jelali and A. Kroll: "Hydraulic Servo-Systems: Modelling, Identification and Control", *Springer*, London, 2003.

[34] H. Demuth and M. Beale: "Neural Networks Toolbox User's Guide: For use with MATLAB", *The MathWorks, Inc*, Massachusetts, 2002.

[35] F. S. Mjalli and S. Al-Asheh: "Neural-Networks-Based Feedback Linearization versus Model Predictive Control of Continuous Alcoholic Fermentation Process", *Chemical Engineering Technology*, Vol. 28, No. 10, pp. 1191 - 1120, October 2005.

[36] K. K. Ahn, H. P. H. Ahn and N. T. Kiet: "A Comparative Study of Modelling and Identification of the Pneumatic Artificial Muscle (PAM) Manipulator based on Recurrent Neural Networks", *Proceedings of the International Symposium on Electrical and Electronics Engineering*, HCM city, Vietnam, 2007.

[37] Q. Zhang and L. Ljung: "Multiple Steps Prediction with nonlinear ARX Models", *Proceedings of the Symposium on nonlinear Control Systems (NOLCOS)*, Stuttgart, Germany, 2004.

[38] M. H. F. Rahiman, M. N. Taib and Y. M. Salleh: "Selection of Training Data for Modelling Essential Oil Extraction System using NNARX Structure", *Proceedings of the International Conference on Control, Automation and Systems*, Seoul, Korea, 2007.

[39] M. T. Hagan, H. B. Demuth and O. Jesus: "An Introduction to the use of Neural Networks in Control Systems", *International Journal of Robust and nonlinear Control*, Vol. 12, No. 11, pp. 959 - 985, September 2002.

[40] S. Haykin, S: "Neural Networks and Learning Machines", Pearson Education, Inc, New Jersey, 2009.

[41] J. Žilková, J. Timko and P. Girovský: "Nonlinear System Control Using Neural Networks", *Acta Polytechnica Hungrica*, Budapest, Hungary, 2006.

[42] A. O'Dwyer: "Handbook of PI and PID Controller Tuning Rules", Imperial College Press, London, 2006.

ERROR SOURCE IDENTIFICATION AND STABILITY TEST OF A PRECISION CAPACITANCE MEASUREMENT SYSTEM

S. Nihtianov* and X. Guo* #

* *Electronic Instrumentation Lab, Faculty EEMCS, Delft University of Technology, Mekelweg 4, 2628CD, the Netherlands. E-mail: S.Nihtianov@tudelft.nl*
# *VSL, Dutch Metrology Institute, Thijsseweg 11, 2629 JA Delft, the Netherlands. E-mail: xguo@vsl.nl*

Abstract: An experimental study is reported for low-frequency noise behavior and identifying the error source of a capacitance measurement system. A test set-up and a special test strategy for this measurement were applied to differentiate between the kinds of external low-frequency interference. The set-up and strategy allowed accurate measurement of the low-frequency component of the intrinsic input noise of the capacitance measurement system. The capacitance measurement system reported was found in the study along with an extremely low value for the low-frequency (1/f) noise with a corner frequency of 2 mHz, and a very high thermal stability of 2 ppm/K, which confirm the design target of this capacitance measurement system.

Key words: Measuring capacitor, low-frequency noise, stability, drift, humidity dependency.

1. INTRODUCTION

Capacitive sensors are popular in industry for displacement measurement, acceleration measurement, pressure measurement, etc. Such a measurement concept can be realized in a simple way and it performs well. In [1] a fast measurement system for capacitance is reported which is intended to be used as interface for multi-channel capacitive sensors with a maximum capacitance of 1pF. The capacitor measurement system is designed to fit the requirements for the continuous measurement of capacitance with high accuracy, yet without the need for periodic calibration [1]. The requirements are namely a very high level of stability and extremely low drift in time and with environmental conditions. The system level design of the charge measurement system can be found in Figure 1.

The measurement is performed by applying an excitation voltage ΔU at the unknown capacitance C_{xi} and measuring the stored charge Q_x in the voltage. The unknown charge Q_x is amplified 50 times by an input charge amplifier and is summed with a reference charge Q_N with opposite polarity, which is generated in a reference charge generator. The sum ΔQ is fed to an integrator. The output voltage of the integrator U_{int} is monitored with a comparator. The state of the comparator controls the reference charge generator and holds the integrator output at 0V. This condition is achieved when the reference charge is equal to the amplified input charge. When the amount of the reference charge has been determined, the gain of the input amplifier and the excitation reference voltage are known, the value of the unknown capacitance is defined. The role of the clock is to accurately define the value of each charge quant which builds up the reference charge. The control logic modifies the contents of the charge-counter every time a charge quant is added or removed from the reference charge.

The measurement is executed in two cycles using both directions of the excitation voltage change. In this way, the input offset voltages and the low-frequency noise of the input amplifier and the integrator are cancelled. The excitation voltage generator and the reference charge generator use a common voltage reference. Therefore, slow variations in the reference voltage do not influence the accuracy of the measurement system [2].

With this principle of operation, the measurement system should have an excellent performance with regard to long-term stability. The reference components of the transfer function are time, the absolute value of one resistor, and the ratio between resistor pairs. All these components are very stable over both temperature and time [2].

However, previous applications of the capacitance measurement system showed drift of the output signal over time and out-of-spec 1/f noise, which should not be there. Thus, a systematic and experimental study of the capacitance measurement system was carried out in order to identify the errors source of such drift and 1/f noise. A new test set-up and test routine were created and applied to reduce the different kinds of interference from the environment to a minimum, which helps in identifying the possible cause of the intrinsic drift and 1/f noise.

For our measurement, the performance of our test set-up was first thoroughly investigated with respect to reference stability, EMI effects, temperature control, and vibration. Numerous tests with modifications of the set-up helped to identify and largely minimize the sources of drift mentioned above.

Next, we investigated the temperature behavior of the capacitance measurement system. A negative temperature coefficient was measured by applying a proper temperature swing.

Copyright © 2009 IEEE: An earlier version of this paper was first published in AFRICON '09, 23-25 September 2009, Nairobi, Kenya

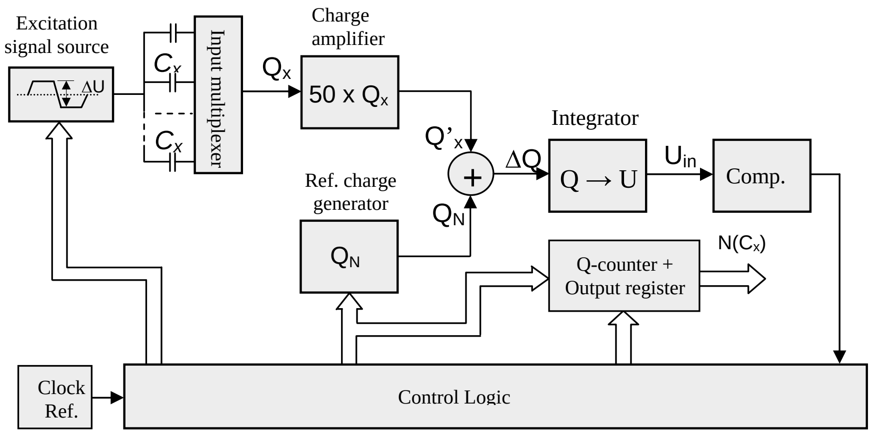

Figure 1. The capacitance measurement system.

This paper provides a demonstration of the test set-up and the most important test results related to the low-frequency noise and the stability. The test results confirm the excellent performance of the capacitance measurement system, which is in agreement with the design targets. A discussion of the test results is also given.

2. TEST STRATEGY AND METHODS

Since thermal stability and 1/f noise were the point of interest in this investigation, a long-term test and a test with temperature variation was required.

Usually when the intrinsic noise of an electronic circuit is measured, the input of the electronic circuit (which is most sensitive to interference) is short-circuited to avoid any external interference, after which the noise at the output of the circuit is measured. This approach is applicable in amplifiers using the so-called "chopping technique", which eliminates the low-frequency component of the input noise and the input drift [3,4]. The principle of operation for the capacitance measurement system also incorporates a kind of chopping technique. However, the realization of this chopping technique requires the use of an external capacitor plus an excitation signal, meaning that the input-noise cannot be measured simply by short-circuiting the input of the system. On the contrary: we have to cope with potentially significant sources of drift (the external capacitor) and a path for external interferences (the cables used to connect the external capacitor to the input of the capacitance measurement system). The main objective of the selected test strategy is therefore to reduce to minimum the effect of these external components on the measurement result.

Figure 2 presents the basic measurement set-up. The set-up includes the DUT (device under test, i.e. the measurement system being tested), an external reference capacitor, and a computer to process the output data. The reference capacitor consists of two parallel plates and is placed in an oven where the temperature and the humidity level can be either programmed or controlled manually (see Figure 3). The value of the reference capacitor is 0.5 pF, which is in the middle of the measurement range of the DUT. In order to make the reference capacitor insensitive to the variation of the temperature in the oven around its set value, aluminum blocks with a large thermal capacitance are placed around it. The capacitor is connected to the measurement system using twisted and shielded wires in order to avoid external interference. Finally, with the help of Pt-100 sensor, the temperature of the capacitive sensor is measured.

The capacitance measurement system is placed in another oven, where the temperature can also be monitored and controlled by computer (see Figure 4). The analog front-end of the system (charge amplifier) is most sensitive to temperature variations, which is why another aluminum block is attached to the charge amplifier in order to increase the thermal constant and to stabilize the temperature. At the same time, this aluminum block improves the immunity of the analog component to electromagnetic interference. Temperature sensors are mounted on the board being tested to monitor the temperature change during the tests.

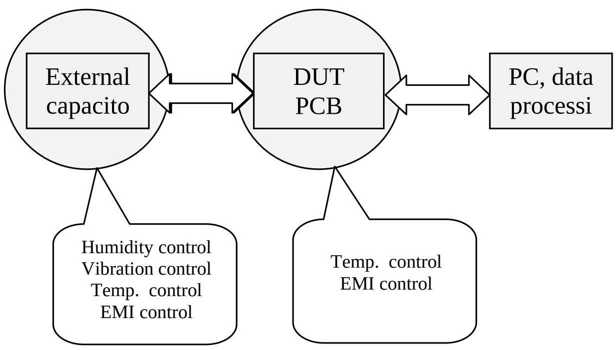

Figure 2. Basic measurement set-up.

Figure 3. The external reference capacitor in an oven encapsulating an Al block with vibration dumping.

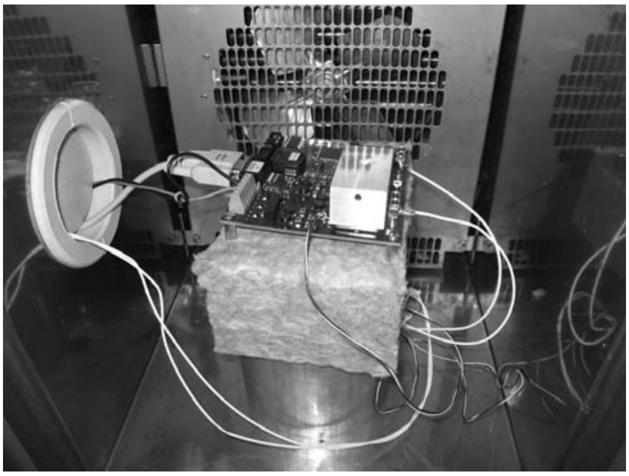

Figure 4. Photo of the capacitance measurement system PCB board in a second oven. An Al block additionally stabilizes the temperature of the input stage.

The measurement system (DUT) is connected to a computer, where control, data acquisition and data processing are performed. For the noise test, the power spectrum density of the measurement data is extracted to see whether it meets the specifications; for the long-term stability test, a moving average of 10,000 samples is applied, which increases the resolution and allows monitoring of the temperature behavior of the capacitance measurement system.

Two types of experimental studies of the DUT were performed: (1) a study of the 1/f noise and (2) a study of the long-term stability. For the study of the noise behavior, special attention was paid to the mechanical vibration of the set-up, since extremely small capacitance values are measured. Any vibration in the set-up may cause relative displacement of the two plates of the reference capacitor, and consequently generate noise at low frequencies, which is exactly the frequency band of our interest. Therefore, a vibration absorption structure was added to the set-up which mainly focuses on the reference capacitor. To test the dumping effect of the anti-vibration structure, experiments with and without vibration absorption were performed, and the results are presented in the next section.

Another issue with regard to the low-frequency noise experiment is the temperature control of the DUT. Since the effect of self-heating cannot be ignored, the DUT has to be placed in a temperature-stable environment to achieve accurate results.

During the experimental study of the long-term stability and the temperature coefficient of the DUT, attention was paid to the control of the humidity of the environment for both the board and the reference capacitor. The relative humidity was maintained at a constant low level throughout the test, since an increase in the humidity level can affect the value of the reference capacitor and the DUT itself.

Electromagnetic interference (EMI) can also be a source of noise. To prevent this from happening, the two Pt-100 temperature sensors, which were placed in the reference sensor and on the DUT, were electrically shielded. Additionally, the oven acted as a shield for the DUT.

3. EXPERIMENTAL RESULTS

3.1 Preliminary tests

A number of preliminary tests were performed to identify and consequently eliminate or control the effect of external disturbing factors like mechanical vibration, humidity, and temperature variation in the noise performance of the DUT.

Mechanical vibration: One of the ‘prime suspects’ for the external contribution to the 1/f noise of the DUT was the susceptibility of the external reference capacitor to mechanical vibrations. To check the efficiency of the applied vibration dumping, two measurements were performed: one measurement with mechanical vibration suppression of the oven and the other without. A comparison of the results with and without mechanical vibration suppression is shown in Figure 5. The plot in Figure 5a is the power spectrum density (PSD) of the output noise without vibration control in the test set-up, while the plot in Figure 5b is the output PSD with vibration control in the test set-up. From this comparison it can be concluded that the small vibration of the oven does contribute to the low-frequency noise, since the plot on the left has a PSD noise level that is one order of magnitude higher in the low-frequency range. Since the focus is only on the low-frequency (i.e., 1/f) behavior resulting from the moving averaging of 10,000 samples at the output, the “noise floor” in Figure 5 cannot be seen.

Thermal effect and thermal stability: The next experiment focused on the thermal stability of the DUT. The temperature behavior of the DUT was tested by applying a temperature swing to the board and recording the output data. The result is presented in Figure 6.

The plot in Figure 6a shows the temperature swing in the oven, while the plot in Figure 6b shows the respective temperature of the DUT recorded by the Pt-100 temperature sensor. Since an aluminum block was added to the board, a thermal filtering effect was demonstrated. The time constant of the thermal filter is clearly larger than the period of the temperature swing applied, which results in a smoothing of the temperature swing. The plot in Figure 6c shows the output signal of the DUT during the temperature swing. There is a clear correlation between the temperature change and the variation of the output signal. From the experimental results presented above, a temperature coefficient of less than -2 ppm/K was calculated by dividing the relative variation of the output signal of the DUT by the value of the thermal swing. The obtained result demonstrates very good thermal stability of the board.

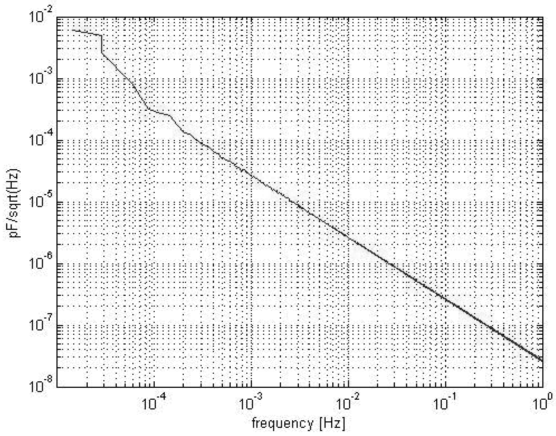

a)

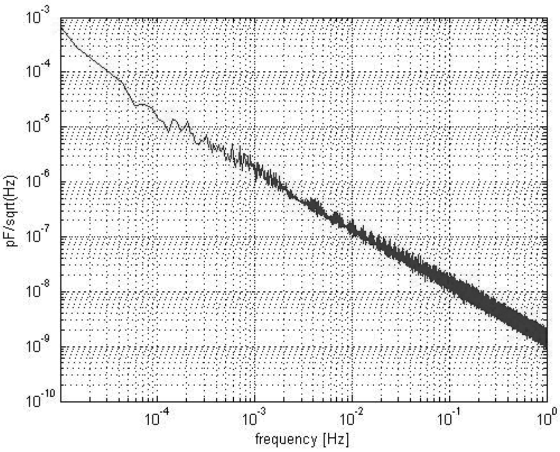

b)

Figure 5. PSD of the measured output noise (a) with and (b) without vibration suppression of the set-up.

We conducted a similar temperature-variation test with the reference capacitor. The measured thermal coefficient of the capacitor was 0.7aF/K.

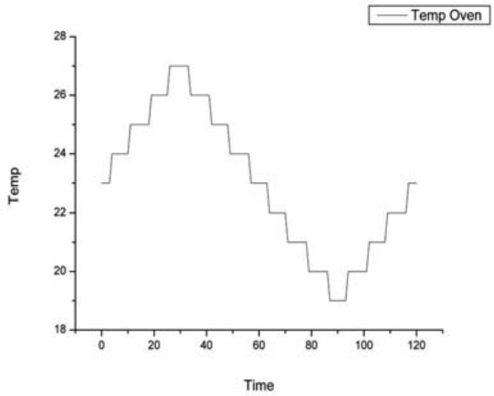

a)

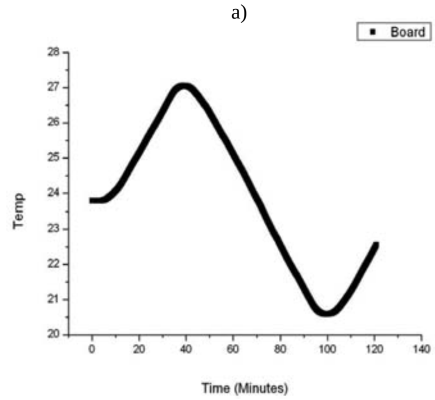

b)

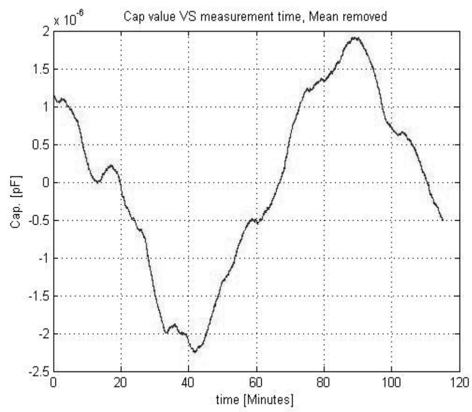

c)

Figure 6. Thermal behaviour of the DUT: (a) temperature swing in the oven; (b) respective temperature swing of the DUT; (c) output signal of the DUT during the temperature swing.

Humidity effect: Relative humidity (RH) variation of the measurement environment may have an effect on both the external reference capacitor and the DUT, even when the temperature is constant. Two experiments were performed at a fixed temperature for both the reference capacitor and the DUT. In one experiment, the relative humidity was varied from 30% to 50% and back to 30% in the oven where the reference capacitor was conditioned (see Figure 7). In the second experiment, the relative humidity in the oven of the DUT was varied from 30% to 40%, and again back to 30% (Figure 8).

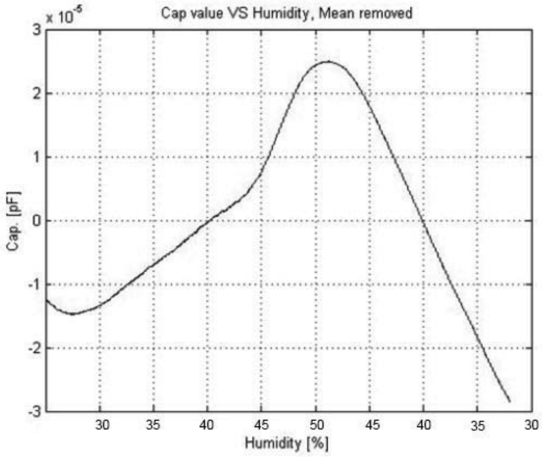

Figure 7. Corresponding change of the measured capacitance with the relative humidity swing of the reference capacitor from 30% to 50% and back to 30%.

There is a clear correlation between the relative change in humidity and the change in the measured capacitance value. The sensitivity to humidity variation of the reference capacitance extracted from Figure 7 is 3aF/1%RH.

In this second experiment, we could not identify a correlation between the relative humidity change and the change of the measured capacitance value (see Figure 8). First, when the humidity increased, the output signal of the DUT also increased. However, it did not decrease when the humidity returned to its original level. Considering the extremely low variation of the measured capacitance during this experiment and the lack of correlation between the input signal (humidity) and the measured capacitance variation, we can assume that what we measured in this case was just a noise. The conclusion we can make is that the sensitivity of the PCB to humidity variation of the reference capacitance is less than 0.2aF/1%RH.

Measurement of 1/f noise: For this last experiment, all measures were taken to stabilize the test environment and to avoid external interferences.

A long-term test was performed to measure the low-frequency input noise of the DUT. All the techniques

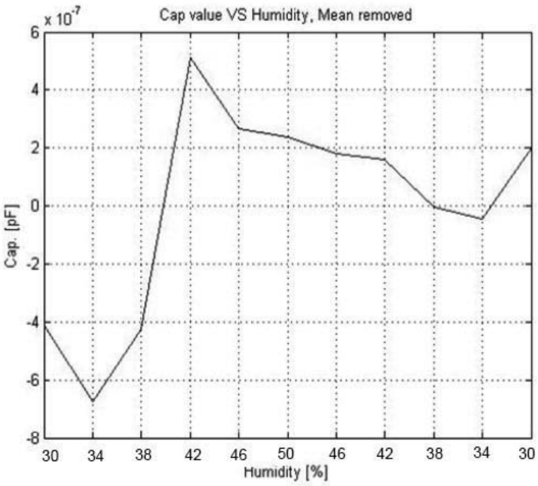

Figure 8. Measured capacitance during changing the relative humidity in the oven of the DUT, from 30% to 50%, and then back to 30%.

mentioned above – vibration control, temperature control, EMI control, and humidity control – were used to avoid any effects of environment instability on the noise measurement result. The duration of the tests was 100 hours. The variation of the temperature during this test of both the DUT and the reference capacitor was 0.2 K. The generated noise due to the temperature variation of the PCB, keeping in mind the result in Figure 6, was less than 0.1aF. The noise contribution of the temperature variation of the reference capacitor was less than 0.2 aF. As can be seen from Figure 9, both values are well below the white-noise floor of the measured noise.

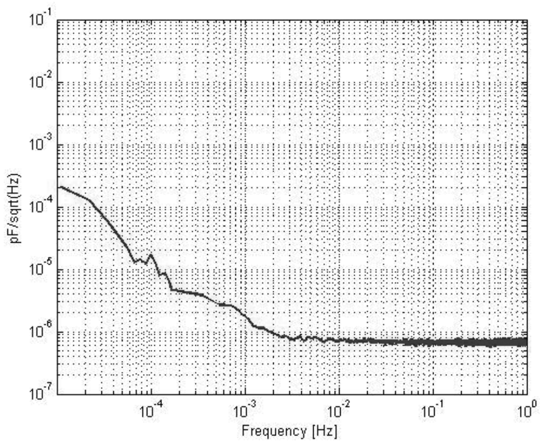

Figure 9. Long-term measurement result, where all technique of reducing external interference are applied.

During the last test, the variation of the humidity of the reference capacitor was less than 0.2%. With the help of the result presented in Figure 7, we calculated the noise contribution of the humidity variation, which was 0.6 aF, which is also below the value of the measured white-noise. The humidity variation of the DUT during the 1/f noise tests was within 0.5%. The contribution of this noise source was only 0.1 aF.

The power spectral density (PSD) of the measured data is presented in Figure 9. The measured noise floor was in the range of 1aF. The corner frequency of the 1/f noise was about 2 mHz, which is a very good result.

4. CONCLUSION AND DISCUSSION

In this paper a systematic test strategy for a capacitance measurement system was presented together with the test results. From the entire test procedure we can conclude that the DUT performs much better than what was concluded from previous tests results.

Any small variations in the environment, such as temperature, humidity, or vibration, will affect the measurement result mainly caused by the external reference capacitor instability.

By reducing the level of instability caused by external factors below the white-noise floor, a 2mHz 1/f-noise corner frequency was measured.

With regard to the thermal stability of the DUT, the tests showed a thermal coefficient of less than 2 ppm/degree, which is a very good achievement.

A valid question is: where, after all, is the residual 1/f noise coming from, after the chopping technique has been applied? In our opinion, there are three possible sources:

1) The presence of 1/f noise in the excitation signal of the DUT, which cannot be reduced by the chopping technique;
2) Parasitic signal paths on the PCB board of the capacitance measurement system;
3) The reference capacitor. Environmental dependence of the capacitance value is expected to have at least three contributions: a) relative dielectric permittivity b) mechanical effects and c) surface layers on the capacitor electrodes. Given the small frequency dependence of the dielectric constant of air, and the small mechanical effect as mentioned above, we thus relate this to surface effects, i.e., the adsorption and desorption of water on the surface. In [5], it is found that this layer will result in a strong frequency dependency of the capacitor, and will lead to a different humidity co-efficient at different frequencies. This frequency dependence is an important error source and should not be included in the 1/f noise contribution of the DUT.

This performance of the capacitance measurement system allows it to be used in applications where long-term measurements need to be performed without intermediate calibrations. For example, one such application is in space to measure very slowly changing displacements caused by fundamental universal phenomena.

More experiments will be conducted in the future to try to locate the main sources of the remaining low-frequency noise and to further improve the performance of the DUT.

REFERENCES

[1] R. Nojdelov, S. N. Nihtianov and E. van Doren, “A fast charge-meter for interfacing capacitive sensors”, *Proceeding of IEEE Africon 2007*, pp. 1-6, September 2007.

[2] R. Nojdelov, S. Nihtianov, “Capacitive-sensor interface with high accuracy and stability”, *IEEE Transactions on Instrumentation and Measurement*, 58 (5), pp. 1633-1639, 2009.

[3] J. F. Witte, K. A. A. Makinwa and J. H. Huijsing, “A CMOS chopper offset-stabilized opamp”, *IEEE Journal of Solid-State Circuits,* vol. 42, no. 7, pp. 1529-1535, July 2007.

[4] K.A.A. Makinwa, M.A.P. Pertijs, J.C.V.D. Meer and J.H. Huijsing, “*Smart sensor design: The art of compensation and cancellation*” ESSDERC 2007 - Proceedings of the 37th European Solid-State Device Research Conference, art. no. 4430884, pp. 76-82. 2008

[5] G. Rietveld and H. E. van den Brom, “DC and low-frequency humidity dependence of 20pF air-gap capacitor”, *IEEE transaction on instrumentation and measurement*, vol. 58, no. 4, April 2009.

Notes